Available online at www.sciencedirect.com
ScienceDirect
Trans. Nonferrous Met. Soc. China 34(2024) 2393−2414
Transactions of Nonferrous Metals Society of China
www.tnmsc.cn

Effect of ultrasonic and mechanical vibration treatments on evolution of Mn-rich phases and mechanical properties of Al−12Si−4Cu−1Ni−1Mg−2Mn piston alloys

Bo LIN[1], Xiang-xiang HE[1], Song-chao XIA[1], Hua-qiang XIAO[1], Yu-liang ZHAO[2,3], Khashayar KHANLARI[4]

1. School of Mechanical Engineering, Guizhou University, Guiyang 550025, China;
2. School of Mechanical Engineering, Dongguan University of Technology, Dongguan 523808, China;
3. Centro Nacional de Investigaciones Metalúrgicas (CENIM), C.S.I.C., Avda. de Gregorio del Amo 8, Madrid 28040, Spain;
4. Department of Chemical & Biotechnological Engineering, Université de Sherbrooke, Québec, QC J1K 2R1, Canada

Received 23 February 2023; accepted 15 July 2023

Abstract: Effects of ultrasonic vibration (UV) and mechanical vibration (MV) on the Mn-rich phase modification and mechanical properties of Al−12Si−4Cu−1Ni−1Mg−2Mn piston alloys were investigated. The results show that the UV and UV+MV treatments can significantly refine and fragmentize the microstructures. In addition, UV treatment can significantly passivate the primary Mn-rich $Al_{15}Mn_3Si_2$ intermetallics. The formation mechanisms of refinement and passivation of the grains and non-dendrite particles were discussed. Compared with the gravity die-cast alloys, the UV and UV+MV treated alloys exhibit improved tensile and creep resistance at room and elevated temperatures. These results can be attributed to the refinement of the α(Al) grains and the secondary intermetallics, the increased proportion of refined heat-resistant precipitates, and the formation of nano-sized Si particles. The ultimate tensile strength of the UV treated alloys at 350 °C exceeds that of commercial piston alloys. This indicates the high application potential of the developed piston alloys in density diesel engines.

Key words: Al−Si piston alloys; Mn-rich phases; mechanical properties; ultrasonic vibration; mechanical vibration

1 Introduction

Eutectic Al−Si−Cu−Ni−Mg alloys are commonly used to manufacture piston parts due to their lightweight, superior castability, excellent wear, and heat and corrosion resistance properties [1−3]. However, due to the high compression and engine efficiency in high power density diesel engines used in the marine and military fields, Al−Si−Cu−Ni−Mg piston alloys can experience temperatures of up to 350−400 °C [4,5]. Therefore, using common eutectic Al−Si−Cu−Ni−Mg alloys as piston alloys in high-power-density diesel engines is an enormous challenge.

Recently, it has been reported that adding Mn is an effective method to improve the mechanical properties of eutectic Al−Si−Cu−Ni−Mg piston alloys. This method is attributed to the formation of heat-resistant Mn-rich phases, such as $Al_{11}Cu_5Mn_3$, $Al_{20}Cu_2Mn_3$, $Al_{15}(MnFe)_3Si_2$, $Al_{15}Mn_3Si_2$, and $Al_{13}Mn_4Si_8$ phases, in the microstructure of such alloys [5,6−9]. Nevertheless, the excessive addition of Mn leads to coarse Mn-rich phases in the microstructure of parts; thus, the Mn content should be controlled below 1.2%. To this end, LI

Corresponding author: Bo LIN, Tel: +86-15285049061, E-mail: linbo1234@126.com;
Yu-liang ZHAO, Tel: +86-18819262344, E-mail: zhaoyl@dgut.edu.cn
DOI: 10.1016/S1003-6326(24)66549-0

et al [10,11] developed an Al−12Si−4Cu−2Mn piston alloy and revealed that the formation of dendritic $Al_{15}Mn_3Si_2$ phases was beneficial to the elevated temperature mechanical properties of the manufactured parts. In our previous work [12], Al−12Si−4Cu−1Ni−1Mg−2Mn piston alloys with enhanced high-temperature mechanical properties were processed. However, coarse Mn-rich phases are formed in the microstructure of parts processed under gravity die-cast (GC) conditions. Due to the poor morphology and distribution of these phases and particles, the improvement of the mechanical properties of Al−Si piston alloys with high Mn content is limited. As a result, the morphology and distribution of Mn-rich particles need to be controlled using physical fields.

In recent years, ultrasonic vibration (UV) and mechanical vibration (MV) melt treatments have been widely used to improve the mechanical properties of Al−Si piston alloys by modifying and refining the secondary intermetallics formed in their microstructure [13,14]. Most UV and MV melt treatment research has focused on their effect on grain size, Si particle content, and Ni-containing intermetallics [15−20]. For instance, JUNG et al [15−17] found that both the ultimate tensile strength (UTS) and elongation were increased by UV due to the refinement of the grain size, Si particles, and secondary phases. DONG et al [18] reported that the particle size of the Al_9FeNi and $Al_3(CuNi)$ phases was significantly refined by UV, which further contributed to improving the mechanical properties at 350 °C. ABU-DHEIR [19] et al and BABU et al [20] investigated the effects of MV on Al−Si alloys and reported that the sizes of grains and primary Si particles were significantly refined. Nevertheless, until now, the research on the effects of UV and MV on the morphology of Mn-rich phases is limited, especially regarding the 3D morphology of Mn-rich intermetallics and their contribution to the high-temperature mechanical properties.

To this end, in the present study, UV and MV are introduced into the melting process of Al−12Si−4Cu−1Ni−1Mg−2Mn piston alloys. The evolution of Mn-rich phases and their contribution to the mechanical properties of Al−12Si−4Cu−1Ni−1Mg−2Mn piston alloys are investigated. Moreover, the evolution of the 3D morphology of Mn-rich phases is studied using deep etching and synchrotron X-ray computed tomography (SXCT). The refinement and passivation mechanisms induced by the UV and MV treatments are also investigated. This research study greatly benefits the industrial application of Al−Si−Cu−Ni−Mg piston alloys with Mn addition.

2 Experimental

2.1 Alloy preparation

The raw materials that included commercially pure Al (99.5%) and master alloys (Al−50%Si, Al−50%Cu, Al−10%Ni, Al−10%Mg, Al−10%Mn, and Al−20%Sr), were used to prepare the experimental alloys and samples. Table 1 presents the chemical composition of the experimental parts determined by optical emission spectrometry. The melting procedure of the processed parts can be found in our previous work [12]. The melt temperature was maintained at 730 °C for 30 min. Approximately 10 kg of Al melt was degassed using pure argon to minimize the hydrogen content of the parts. The melts were poured into an H13 mold to obtain the GC alloys (GC parts). Subsequently, the melts were poured into a cup at a temperature of 620 °C (the semi-solid state), treated with UV (MS5s) at 900 W for 2 min, and poured into an H13 mold to obtain the UV-treated alloys (UV parts). The UV treatment melt temperature was selected according to the formation temperature of the $Al_{15}Mn_3Si_2$ phase [10]. Then, the UV-treated melts were poured into an H13 mold under mechanical vibration (MV, ZT-40−20V) to obtain the UV- and MV-treated alloys (UV+MV parts); the vibration frequency was 20 Hz, and the vibration amplitude was approximately 2 mm. Finally, casting parts with 80 mm in height and 50 mm in diameter were obtained. A schematic of the GC, UV, and UV+MV processes is illustrated in Fig. 1.

Table 1 Chemical composition of Al−12Si−4Cu−1Ni−1Mg−2Mn alloys (wt.%)

Si	Cu	Mn	Fe	Ni	Mg	Sr	Al
12.08	3.96	2.05	0.08	1.18	0.93	0.03	Bal.

2.2 Heat treatment and mechanical property test

T6 heat treatment conditions were used to stabilize the microstructure of the processed samples. The samples were solution-treated at 505 °C for 8 h, quenched in warm water at 100 °C, and finally

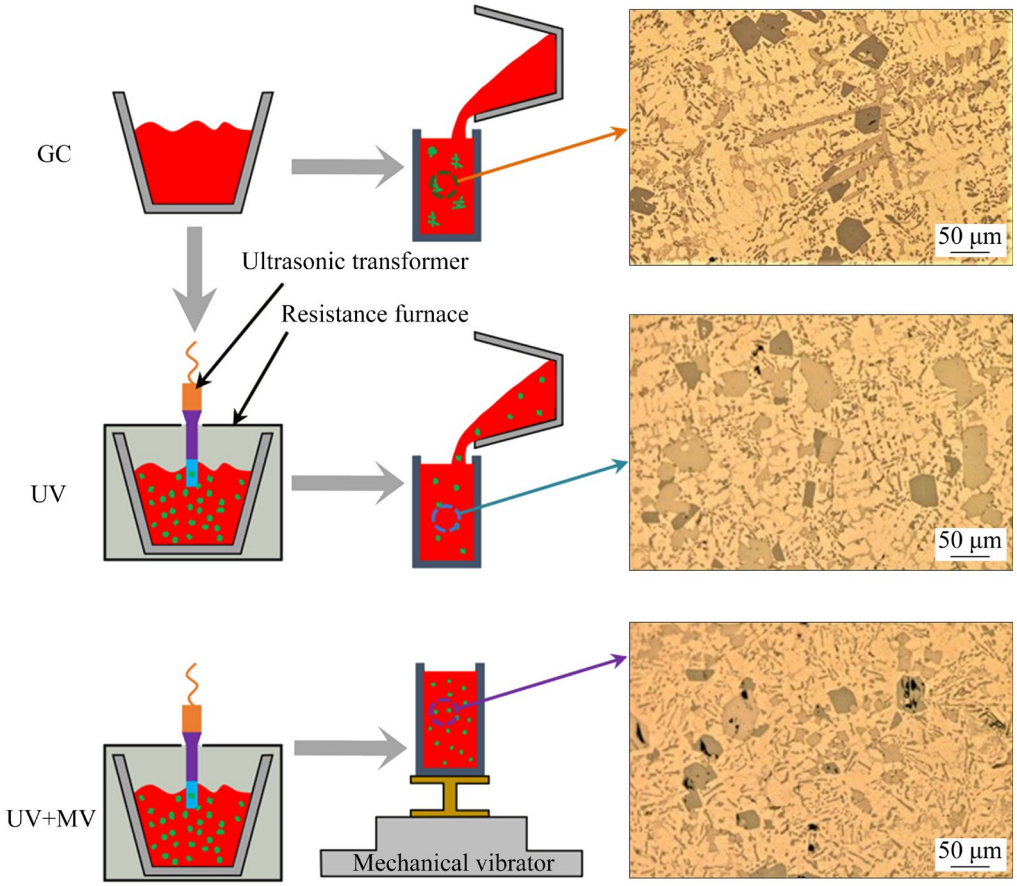

Fig. 1 Schematic of GC, UV and UV+MV processes

aged at 160 °C for 12 h. The room temperature tensile properties were determined using a standard testing machine (MTS CMT5105) at a displacement rate of 1.0 mm/min. High-temperature tensile tests were performed on the same testing machine with a constant-temperature box at an elevated temperature of 350 °C. The heating rate and time to approach 350 °C were 15 °C/min and 0.5 h, respectively, and the displacement rate at this temperature was 1.0 mm/min. The tensile test values obtained from at least five tests were averaged. The uniaxial tensile creep properties were determined with a high-temperature creep testing instrument (RDL50) at 200 °C for 8 h under creep stresses of 50 and 100 MPa, respectively.

2.3 Microstructure and fracture surface observation

Metallographic samples were cut from the clamped part of the tensile test samples and were etched in 0.5% hydrofluoric acid solution for 30 s. Subsequently, the samples were studied by a metallurgical microscope (OM, ICX4IM, Ningbo Sunny Instruments Co., Ltd., China). The metallographic samples and fracture surfaces were analyzed using scanning electron microscopy (SEM, Zeiss Gemini 300, Germany). The sizes of the Mn-rich phases and primary Si particles were calculated using the Image Pro Plus (IPP) software. Since the morphology of the Mn-rich phases exhibited a dendrite form, the equivalent diameter was used to determine their size. The morphology of the secondary intermetallics was observed using energy dispersive spectroscopy (EDS), while the fracture surfaces were observed by scanning electron microscopy (SEM). The polished samples were etched in the iodine−methanol solution (approximately 10 g iodine in 100 mL methanol) to remove the Al matrix. Next, the 3D morphologies of the secondary intermetallics were observed by SEM. The morphology of α(Al) was also observed by electron backscattered scattering detection (EBSD) in SEM. SXCT was also used to reveal the 3D morphology of the secondary intermetallics. The

SXCT experiments were performed at the BL13HB beamline of the Shanghai Synchrotron Radiation Facility, China. Detailed SXCT parameters can be found in our previous work [21]. The 2D slices and 3D morphology of the secondary phases were reconstructed using the PITRE and Avizo software, respectively [22]. The image processing and segmentation procedures are depicted in Fig. 2. X-ray diffraction (XRD) analysis was performed (BrukerAXS D8 ADVANCE, Karlsruhe, Germany) to investigate the phase evolution under different casting conditions. The precipitate particles in the α(Al) matrix were analyzed using transmission electron microscopy (TEM, JEOL JEM-F200, Japan) at 200 kV.

3 Results

3.1 2D microstructure

Figure 3 presents the morphology changes of the Mn-rich intermetallics in UV- and MV-treated parts under T6 heat treatment as characterized by OM and SEM. The EDS results of the Mn-rich phases are presented in Table 2. Although the morphology of the Mn-rich phases was modified by the UV and MV techniques, no change appeared in the EDS results of these Mn-rich intermetallics. The EDS results revealed that the Mn-rich phases are $Al_{15}Mn_3Si_2$ [23]. In addition, the size of the Mn-rich phases and primary Si particles was calculated using the IPP software. In GC alloys, the Mn-rich phases appeared as long dendrites approximately 225 μm in length. In the UV samples, the morphology of the Mn-rich phases changed into small block-like particles with a size of about 75 μm. In the UV+MV-treated samples, the morphology of the small block-like Mn-rich phases was further refined to a size of about 40 μm. Moreover, the size of the primary Si particles in the UV and UV+MV-treated samples also decreased significantly. The size of the primary Si particles in the GC alloys was about 125 μm and became 70 μm in the UV samples and 45 μm in the UV+MV ones.

Figure 4 shows the XRD patterns of the processed Al−Si−Cu−Ni−Mg−Mn piston alloys. All contained α(Al), Si, Al_2Cu, $Al_3(CuNi)$, $Al_5Cu_2Mg_8Si_6$, and Mn-rich phase, i.e., $Al_{15}Mn_3Si_2$. Furthermore, the XRD patterns proved that the applied UV and MV treatments did not alter the type of secondary intermetallics formed in α(Al).

3.2 α(Al) morphology

Figure 5 displays the morphology of α(Al) in the microstructure of parts prepared under different casting conditions. In the GC parts, most of the α(Al) grains exhibited a coarse dendritic shape, and

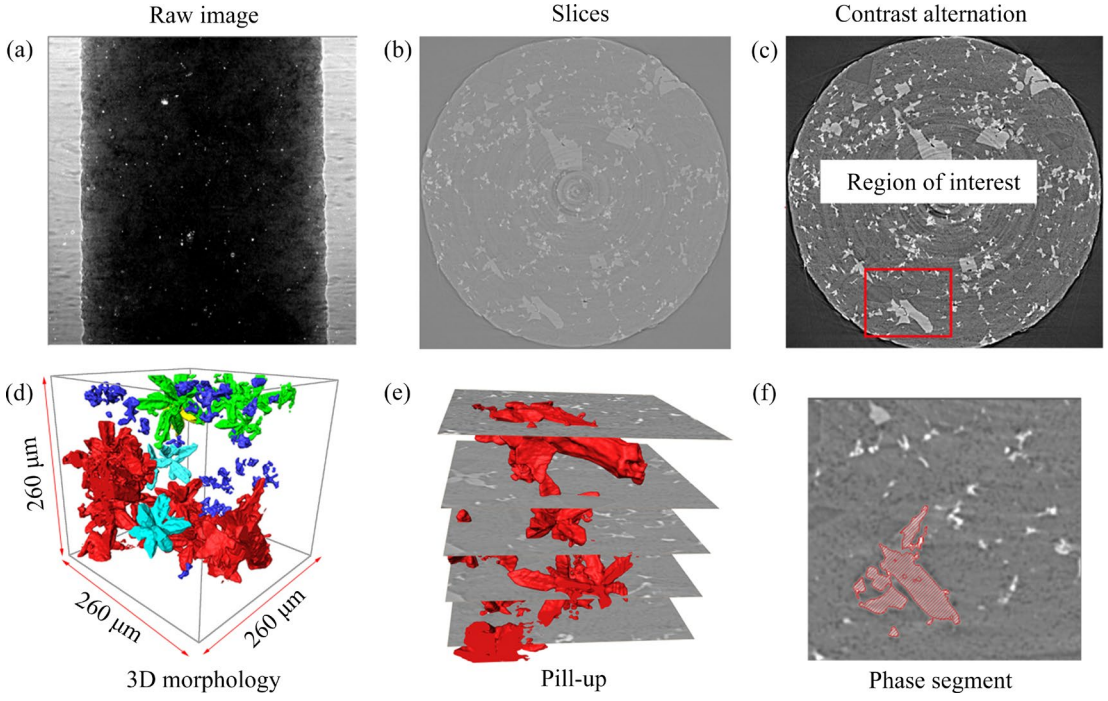

Fig. 2 Image process and segmentation procedure of secondary intermetallics

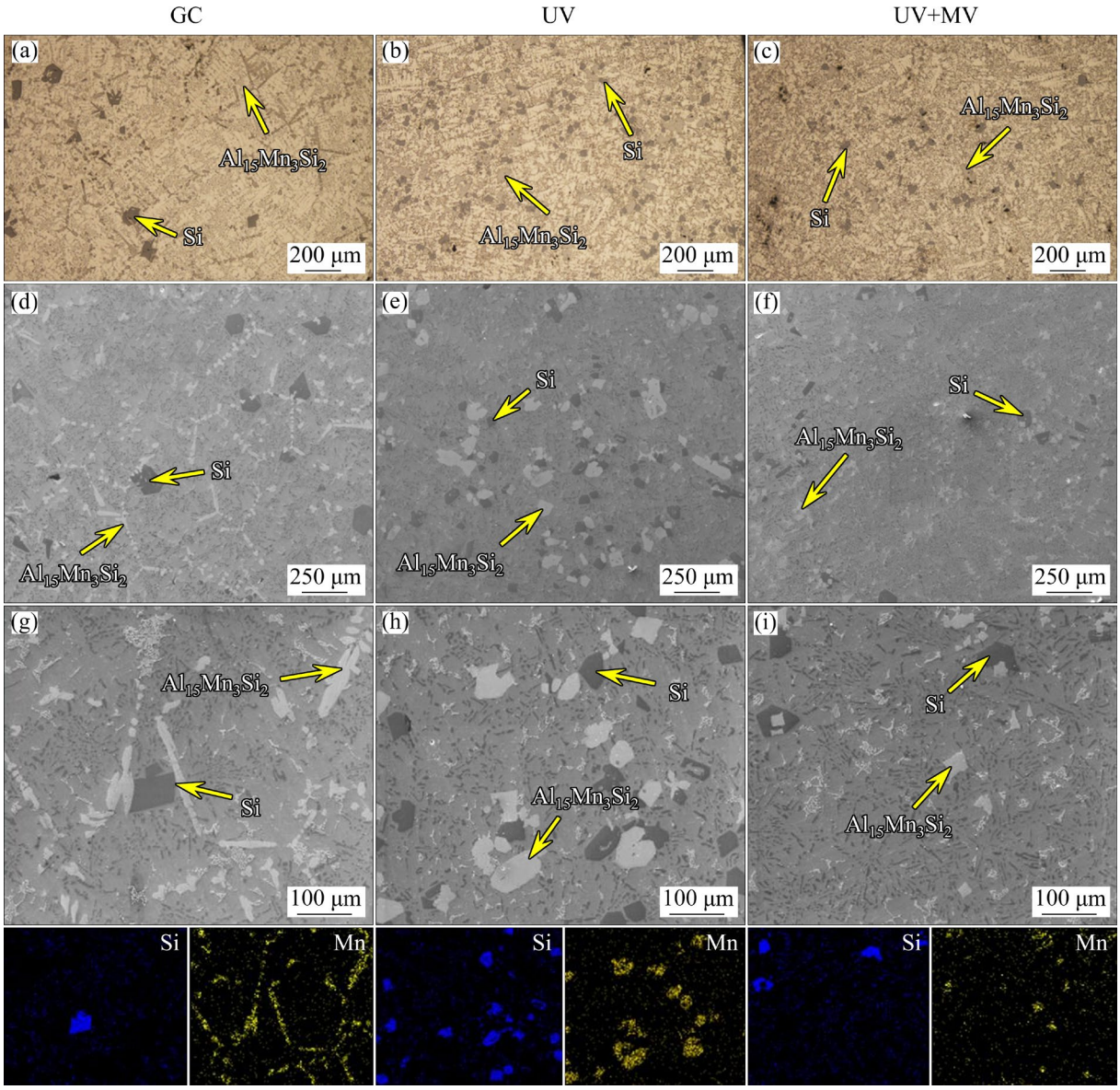

Fig. 3 OM images of alloys under different cast conditions after T6 heat treatment: (a−c) OM images of alloys under GC, UV, and UV+MV treatments, respectively; (d, g) SEM images of alloys under GC treatment; (e, h) SEM images of alloys under UV treatment; (f, i) SEM images of alloys under UV+MV treatment

Table 2 EDS results of Mn-rich phases in piston alloys under UV and MV treatments (wt.%)

Phase	Al	Si	Mn	Cu	Fe	Ni	Source
$Al_{15}Mn_3Si_2$	71.55	14.20	13.58	0.67	−	−	Ref. [23]
$Al_{15}Mn_3Si_2$	69.08	13.35	15.20	0.51	1.27	0.59	GC alloy
$Al_{15}Mn_3Si_2$	68.64	13.70	15.17	0.83	1.13	0.53	UV alloy
$Al_{15}Mn_3Si_2$	67.81	14.03	15.41	0.71	1.47	0.57	UV+MV alloy

the largest grain size was roughly 1000 μm. The UV and UV+MV treatments refined the grain sizes. In the UV-treated alloys, the largest grain size was nearly 500 μm, and in the UV+ MV-treated alloys, it was approximately 400 μm. In addition, according to the OM and EBSD images, the UV and UV+MV treatments significantly fragmented the α(Al) dendrites (as indicated by the arrows).

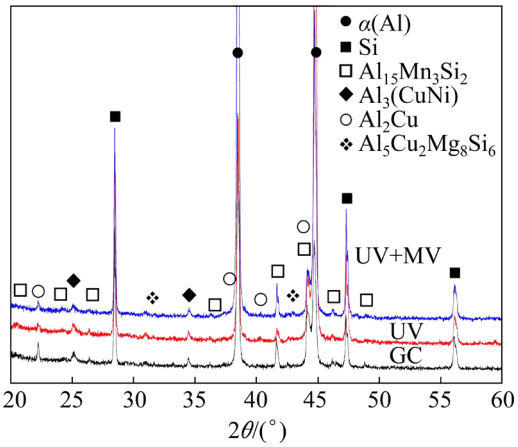

Fig. 4 XRD patterns of alloys under different casting conditions

3.3 3D morphology of intermetallics

Figure 6 reveals the 3D morphology and EDS maps of the secondary intermetallics formed in the GC, UV, and UV+MV samples. In the GC alloys, the Mn-rich $Al_{15}Mn_3Si_2$ particles appeared in coarse dendritic are formed (Fig. 6(a)). Moreover, Al_3(CuNi) exhibits a skeleton-like 3D morphology. Notably, the Al_3(CuNi) particles are formed adjacent to the Mn-rich $Al_{15}Mn_3Si_2$ phases, indicating that the Al_3(CuNi) phase might have been nucleated on the $Al_{15}Mn_3Si_2$ particles. As a result, the modification of the Mn-rich phases caused by the UV and MV treatments is also expected to affect the distribution of the Al_3(CuNi) phases in the parts. Figures 6(b−e) present the 3D morphology and EDS maps of the Mn-rich phases in the UV and UV+MV samples. The Mn-rich $Al1_5Mn_3Si_2$ particles in the UV and UV+MV samples exhibit a block-like 3D morphology, different from that observed in the GC samples. Furthermore, the 3D morphology of the secondary intermetallics is more uniformly distributed in the UV alloys, leading to better connectivity of the network structure of heat-resistant phases compared with that of the GC parts.

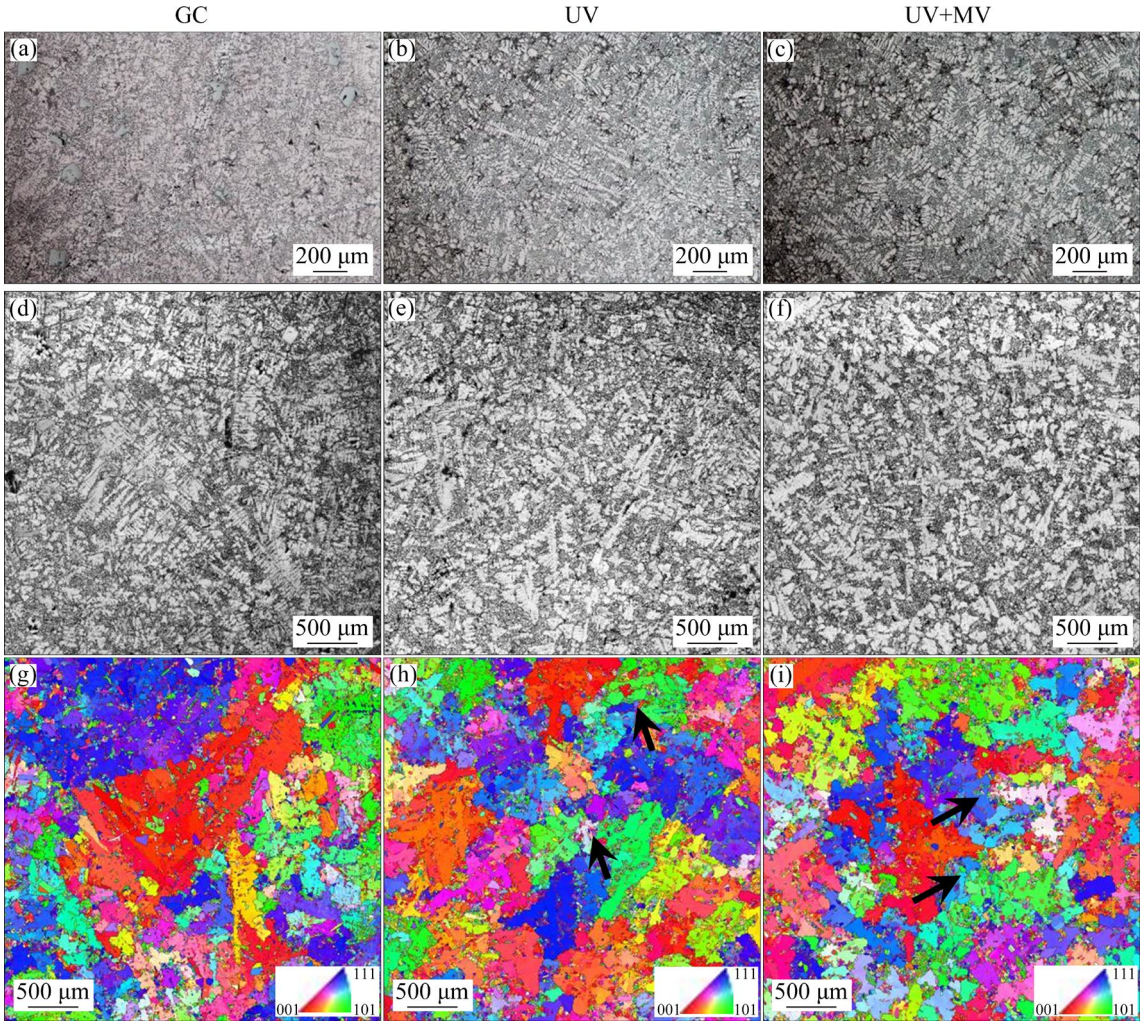

Fig. 5 OM and EBSD images of α(Al) in microstructure: (a−c) OM images; (d−f) IQ images; (g−i) IPF maps

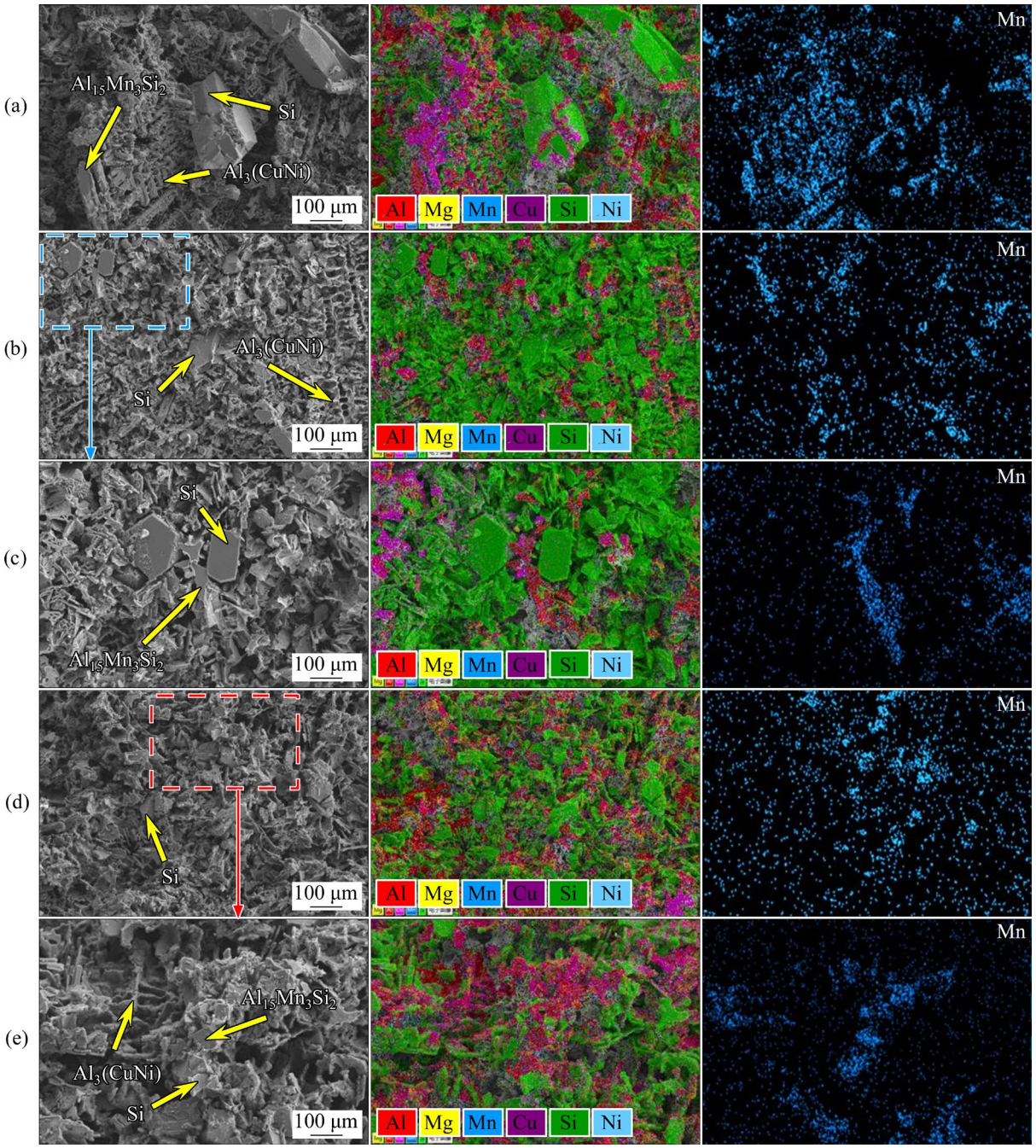

Fig. 6 3D morphologies and EDS maps of secondary intermetallics: (a) 3D morphology of secondary intermetallics in GC alloys; (b, c) 3D morphology of secondary intermetallics in UV alloys; (d, e) 3D morphology of secondary intermetallics in UV+MV alloys

The 3D morphologies of the Mn-rich intermetallics and secondary intermetallics in the GC and UV alloys were obtained by SXCT, and the results are shown in Fig. 7. The Mn-rich intermetallics in the GC parts exhibit a typical dendritic 3D morphology. Compared with that in the GC alloys, the size of the Mn-rich intermetallics is significantly refined in the UV parts (Figs. 7(a, b)). The volume of the largest Mn-rich particles in the GC parts was 690918 μm^3, five times that in the UV parts (134560 μm^3). In addition, the Mn-rich particles in the GC parts appeared as a compact interconnected network structure. Nevertheless, most of the Mn-rich particles formed in the UV parts exhibited a dispersed interconnected network structure, while some of these particles appeared to be distributed separately. Based on the 3D morphology of single Mn-rich particles, it can be

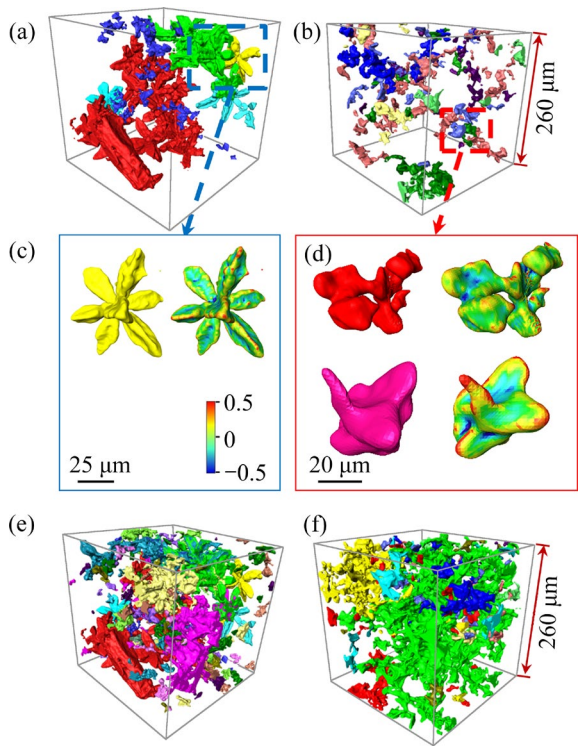

Fig. 7 3D morphologies of Mn-rich intermetallics and secondary intermetallics: (a, c) Mn-rich intermetallics in GC alloys; (b, d) Mn-rich intermetallics in UV alloys; (e, f) Secondary intermetallics in GC and UV alloys, respectively

deduced that the whole dendritic-like structure was fragmented by the UV treatment, losing its initial characteristics (Figs. 7(c, d)). In Figs. 7(c, d), the surface curvature color reflects the shape of the formed intermetallics, i.e., protrusion shape (red color) and concave shape (blue color). It can be observed that the edge of the Mn-rich particles, varying in color from yellow to red, was more significant in the UV samples than that in the GC alloys. This observation indicates that the Mn-rich phases in the UV alloys are rounder than those in the GC alloys. Figures 7(e) and (f) present the 3D morphology of the secondary intermetallics in the GC and UV alloys, respectively. Due to the existence of other intermetallics, i.e., $Al_3(CuNi)$ and eutectic Si particles, the connectivity of the network structure in the UV alloys was more apparent than that in the GC ones.

3.4 Dispersoid particles

Figure 8 reveals the precipitated particle morphology, selected electron diffraction patterns (SADP), and EDS results of the GC samples. The SADP results confirm that the nano-sized needle-shaped precipitated particles were $\theta'(Al_2Cu)$ phase (Figs. 8(a, b)) [24−26]. The EDS results reveal that the needle-shaped precipitated particles contained Al and Cu elements, further confirming that these particles were $\theta'(Al_2Cu)$ (Fig. 8(c)). In addition, the SADP results confirm that the micro-scale rod-shaped precipitated particles were $T(Al_{20}Cu_2Mn_3)$ phase (Figs. 8(d, e)) [27,28]. The EDS results revealed that the needle-shape precipitated particles contained Al, Cu, and Mn elements, further confirming that these particles were $T(Al_{20}Cu_2Mn_3)$ phase (Fig. 8(f)). Two types of nano-sized cubic-shaped precipitated particles were observed in the experimental samples. The SADP results confirmed that one of the two nano-sized cubic-shaped precipitated particle types was α(MnFe)-$(Al_{15}(MnFe)_3(CuSi)_2)$ phase (Figs. 8(g) and (h)). The EDS results suggested that the cubic-shaped precipitated particles contained Al, Mn, Si, Fe, Ni, and Cu elements, further confirming that this phase was α(MnFe)$(Al_{15}(MnFe)_3(CuSi)_2)$. Nano-sized α(MnFe) is often found in Al−Cu, Al−Mn−Fe, and Al−Si alloys [6,29−31]. These findings are consistent with those by LIAO et al [6], who also found nano-sized α(MnFe) in Al−Si−Cu−Mn piston alloys after performing T6 heat treatment. The SADP and high-resolution image results confirmed that the second type of nano-sized cubic-shaped precipitated particles was the $Al_{11}Cu_5Mn_3$ phase (Figs. 8(i) and (j)). Consistent with observations, TIAN et al [5] found nano-particle $Al_{11}Cu_5Mn_3$ formed in Al−Si−Cu−Ni−Mg−Mn piston alloys after performing T6 treatment and re-aging at 350 °C.

Figure 9 demonstrates the TEM images of the matrix in the samples prepared under different casting methods. Compared with that in the GC alloys, dispersoids in the UV+MV and UV parts were significantly smaller. However, it should be noted that their area fraction was dramatically larger. The size and area fraction of dispersoids were quantitatively analyzed, and the results are presented in Fig. 10. The size of $\theta'(Al_2Cu)$ was estimated to be 156.5 nm in the GC alloys, 140.3 nm in the UV alloys, and 110.9 nm in the UV+MV alloys. The size of $Al_{15}Mn_3Si_2$ or $Al_{11}Cu_5Mn_3$ was estimated to be 186.9 nm in the GC alloys, 153.1 nm in the UV alloys, and 98.4 nm in the UV+MV alloys. The size of $T(Al_{20}Cu_2Mn_3)$ was estimated to be within 0.5−1 μm in all samples. The area fractions of

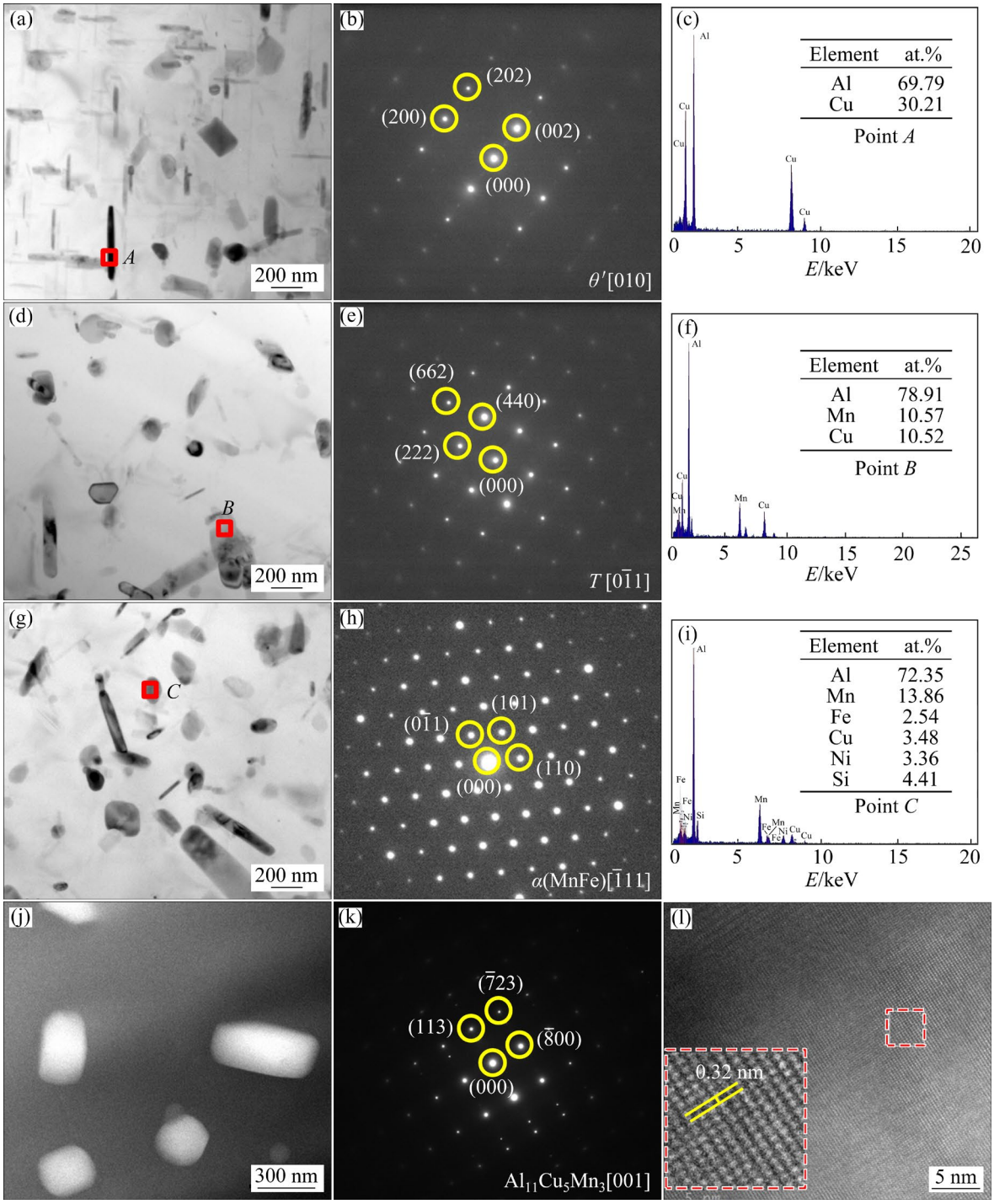

Fig. 8 SADP and EDS results of GC samples: (a) Morphology of θ'(Al_2Cu) phase; (b) SADP of θ'(Al_2Cu) phase; (c) EDS results of θ'(Al_2Cu) phase; (d) Morphology of T phase; (e) SADP of T phase; (f) EDS results of T phase; (g) Morphology of α(MnFe) phase; (h) SADP of α(MnFe) phase; (i) EDS results of α(MnFe) phase; (j) Morphology of $Al_{11}Cu_5Mn_3$ phase; (k) SADP of $Al_{11}Cu_5Mn_3$ phase; (l) EDS results of $Al_{11}Cu_5Mn_3$ phase

θ'(Al_2Cu) and dispersoids were measured to be 6.8% and 21.8% in the GC alloys, 7.4% and 23.3% in the UV alloys, 9.3% and 26.7% in the UV+MV alloys, respectively. It can be concluded that UV and MV refine the dispersoids and increase their number. UV and MV treatments increased the fraction of dispersoids in the Al−Si−Cu−Ni−Mg−Mn alloy, which can be attributed to grain refinement and increased solid solubility of elements [32,33].

Figure 11 exhibits morphologies and EDS results

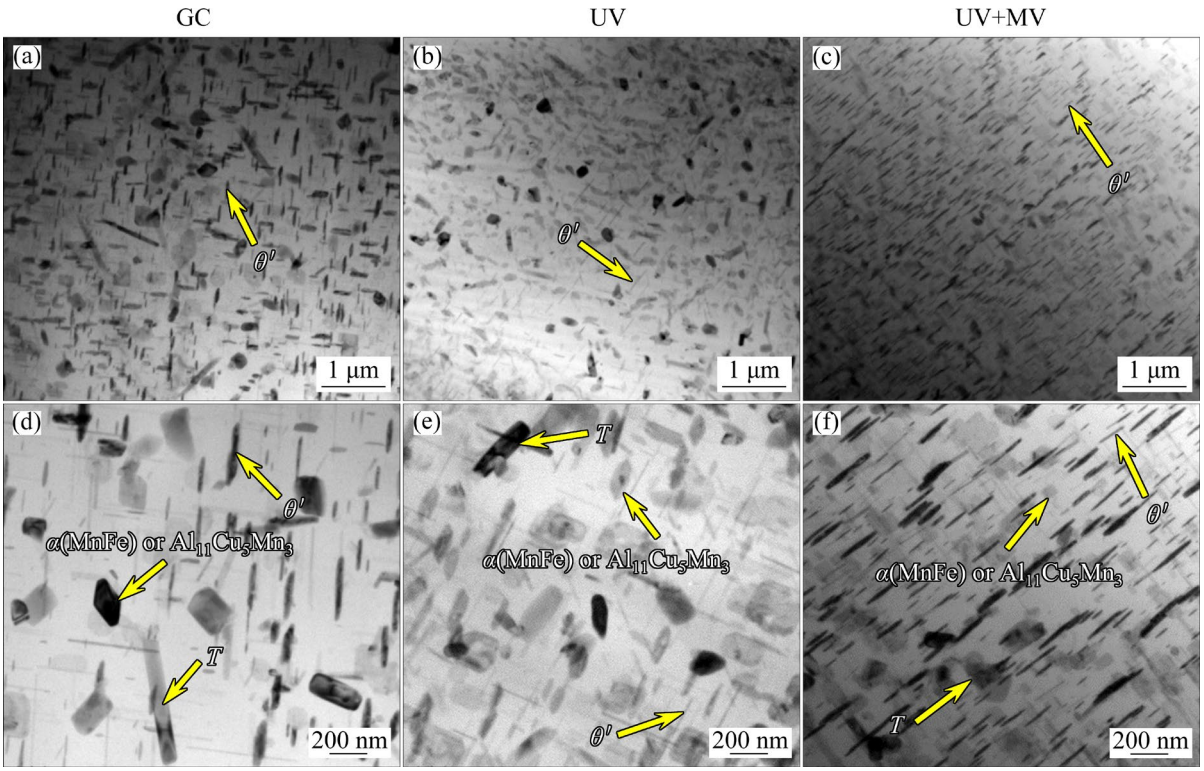

Fig. 9 Precipitated particle morphologies: (a, d) GC alloys; (b, e) UV alloys; (c, f) UV+MV alloys

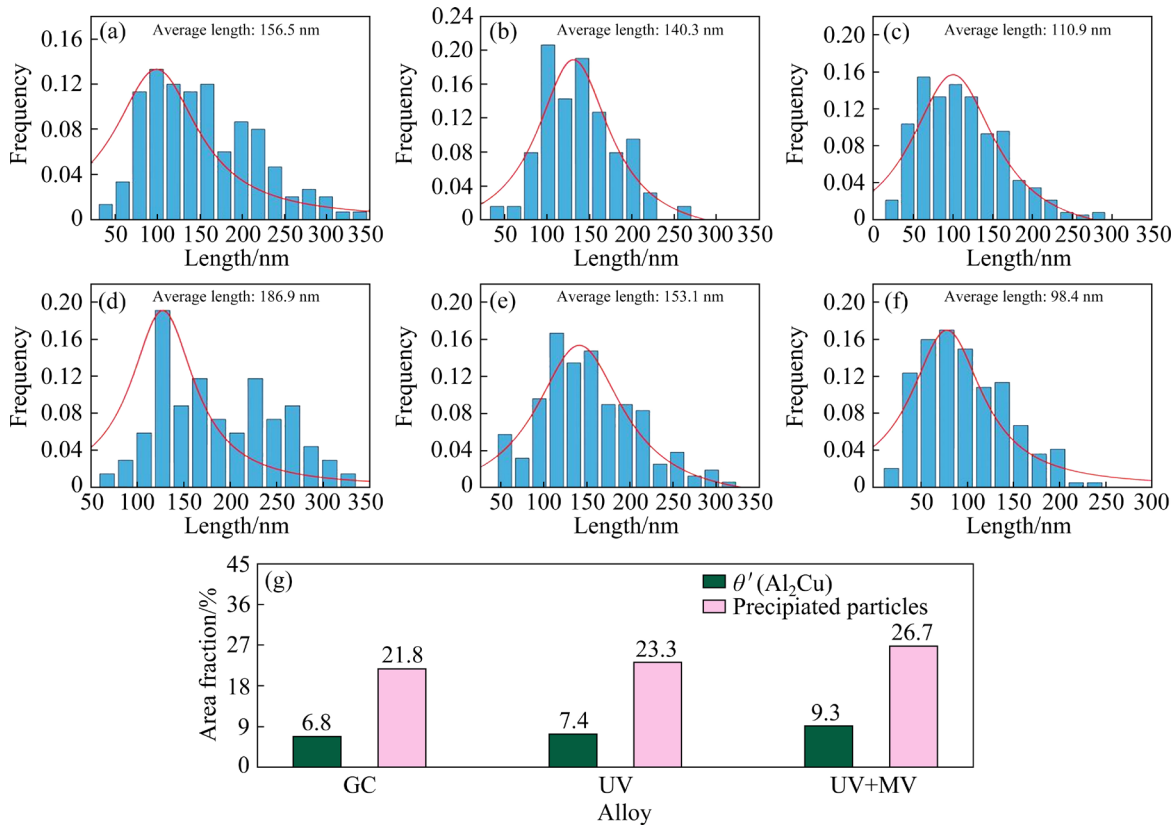

Fig. 10 Size and area fraction of dispersoids: (a−c) Size of $\theta'(Al_2Cu)$ in GC, UV, and UV+MV alloys, respectively; (d−f) Size of $Al_{15}Mn_3Si_2$ or $Al_{11}Cu_5Mn_3$ in GC, UV, and UV+MV alloys, respectively; (g) Area fraction of $\theta'(Al_2Cu)$ and precipitated particles in GC, UV, and UV+MV alloys, respectively

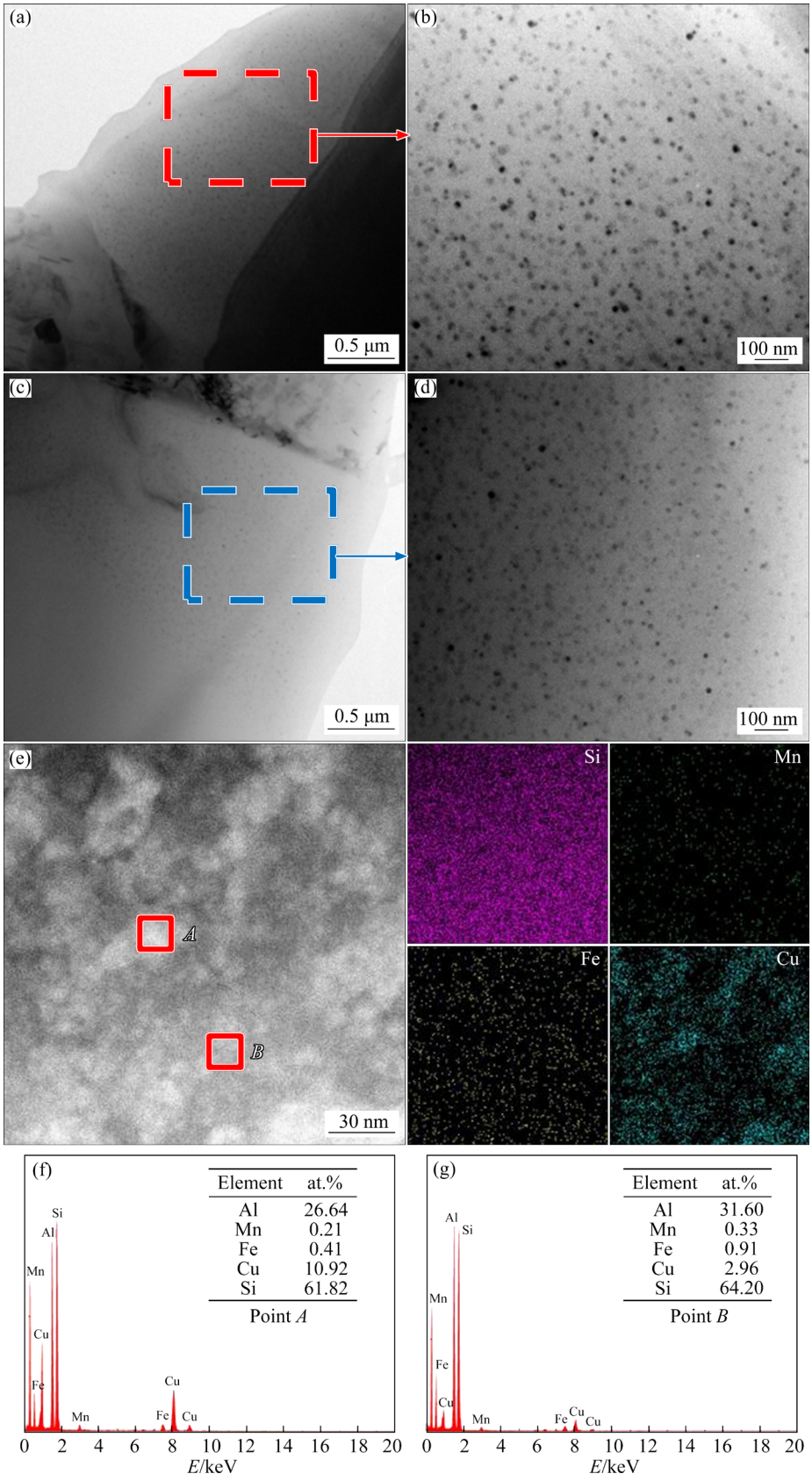

Fig. 11 Morphologies of nano-sized Si particles in UV alloys (a, b) and UV+MV alloys (c, d), high magnification morphology and corresponding EDS mappings of UV+MV alloys (e), and EDS results of Point *A* (f) and Point *B* (g), respectively

of the nano-sized Si particles formed in samples processed under different casting methods. Numerous nano-sized Si particles were found in the UV and UV+MV samples with sizes of about 13 and 10 nm, respectively. WANG et al [34] also reported that nano-sized Si particles were formed in Al−7Si alloys during complex shear flow casting. This observation can be attributed to Al−Si and Si atomic clusters being refined in the Al melt and then captured by the growing Al under stirring conditions [34]. In this study, the UV and MV treatments promoted the growth of Al under a semisolid state or solidification condition, refining Si atomic clusters. Consequently, nano-sized Si particles could be easily formed in the micro-structure of these parts.

3.5 Mechanical properties

Figure 12 presents the mechanical properties of the Al−Si−Cu−Ni−Mg−Mn parts processed under different casting methods. The room temperature tensile testing results reveal that, after UV treatment, the UTS, yield strength (YS), and elongation (EL) increased from 246 to 270, 116 to 150 MPa, and 1.2% to 2.3%, respectively, compared with those of the GC samples. The UV+MV samples exhibited the best tensile properties at room temperature, with their UTS, YS, and EL being 293 MPa, 162 MPa, and 3.3%, respectively. Compared with the tensile properties obtained at the elevated temperature of 350 °C of the GC parts, the UTS, YS, and EL of the UV treatment parts increased from 84 to 113 MPa, 78 to 107 MPa, and 2% to 4.1%, respectively. On the other hand, the UTS and YS of the UV+MV alloys at the elevated temperature of 350 °C decreased compared with those of the UV alloys.

Figure 12(d) depicts the creep curves obtained at a temperature of 200 °C and applied stress of 50 MPa or 100 MPa of the Al−Si−Cu−Ni−Mg−Mn alloys processed under different casting methods. All three types of samples exhibited a similar creep behavior; however, their maximum creep strain demonstrated large difference. Notably, in the GC alloys, the maximum creep strain at a temperature of 200 °C and applied stress of 50 MPa after 8 h reached 0.12%, while the corresponding values in

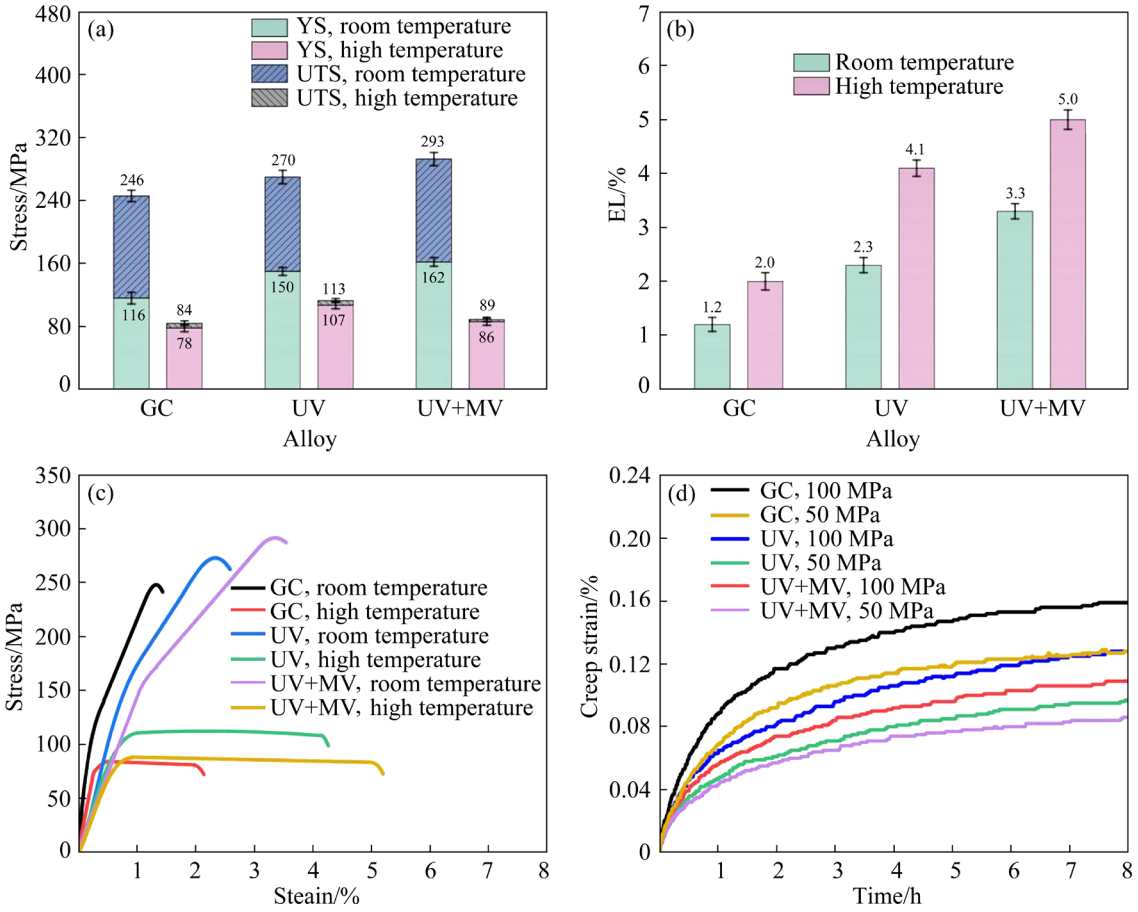

Fig. 12 Mechanical properties of alloys under different casting methods: (a) UTS and YS; (b) EL; (c) Tensile curves; (d) Creep curves

the UV and UV+MV alloys were 0.08% and 0.07%, respectively. In addition, the maximum strain of the three alloys increased significantly when the applied stress was increased from 50 to 100 MPa. The creep results confirm the great improvement in the creep resistance of the parts treated by UV and UV+MV.

The UTS of the Al−Si−Cu−Ni−Mg−Mn parts processed at the elevated temperature of 350 °C under different casting methods was compared to that of commercial Al−Si piston alloys [5,11,15,18，29,35−41], and the results are listed in Table 3. The elevated temperature UTS values of the GC alloys were higher or close to those of the most commercial Al−Si piston alloys. In contrast, those of the UV alloys exceeded those of the commercial Al−Si piston alloys. It should be noted that the elevated temperature UTS value of the alloy after UV treatment was 109.57 MPa in Ref. [18], which is close to that of the UV parts. However, the Ni content in the parts prepared in Ref. [18] was twice that of the UV alloys prepared in this study. It should be mentioned that the more complex composition and the existence of rare earth elements in the parts prepared in Ref. [18] led to a higher processing cost than that of the UV parts processed in this study.

3.6 Fracture behavior

Figure 13 displays the fracture surfaces of experimental alloys prepared under different casting methods tested at 350 °C. Mixed-rupture cleavage and dimples were observed on the fracture surfaces of the three experimental samples. This observation indicates that the brittle and ductile fracture modes coexisted in the processed parts. In addition, no apparent grain sliding was observed in all experimental samples. It is assumed that the 3D co-continuous network structure of the secondary intermetallics prevented grain sliding during the elevated temperature tensile tests. In the GC alloys, cleavage planes and several cracks caused by the coarse Mn-rich phases and primary Si particles were observed on the fracture surfaces. This indicates

Table 3 UTS of Al−Si−Cu−Ni−Mg−Mn alloys under different casting methods compared with that of commercial Al−Si piston alloys at 350 °C

Composition	UTS/MPa	Source
Al−12Si−4Cu−1Ni−1Mg−2Mn(GC,T6)	84	This study
Al−12Si−4Cu−1Ni−1Mg−2Mn(UV,T6)	113	This study
Al−12Si−4Cu−1Ni−1Mg−2Mn(UV+MV,T6)	89	This study
Al−13Si−4Cu−2Ni−1Mg(GC,T6)	88	Ref. [5]
Al−13Si−3.0Cu−0.6Fe−0.6Mn(GC,T6)	85	Ref. [29]
Al−13Si−5.0Cu−0.6Fe−0.6Mn(GC,T6)	88	Ref. [29]
Al−13.0Si−1.08Cu−1.05Mg−1.0Ni(GC,T6)	61.63	Ref. [35]
Al−12.8Si−3.23Cu−1.01Mg−1.0Ni(GC,T6)	61.71	Ref. [35]
Al−12.57Si−1.02Cu−1.23Mg−1.07Ni−0.04Mn(GC,T6)	67.07	Ref. [36]
Al−12.57Si−1.02Cu−1.23Mg−1.07Ni−0.15Mn(GC,T6)	75.62	Ref. [36]
Al−12.57Si−1.02Cu−1.23Mg−1.07Ni−0.40Mn(GC,T6)	71.92	Ref. [36]
Al−12.01Si−3.53Cu−2.12Mn(GC,T6)	83	Ref. [11]
Al−11.75Si−3.16Cu−2.22Ni−0.76Mg−0.12Fe(UV,T6)	60	Ref. [15]
Al−11.45Si−3.78Cu−2.19Ni−0.68Mg−0.48Fe−0.00037P−0.46Cr−0.33RE(UV,T6)	109.57	Ref. [18]
Al−12Si−3.5Cu−2Ni−0.8Mg−0.4Fe−0.15Zr−0.15Ti (GC, T6)	101	Ref. [37]
Al−12.21Si−0.91Cu−0.96Ni−0.69Mg−0.53Mn−0.57Fe−0.28Zn−0.18Ti (GC,T6)	94	Ref. [39]
Al−5.44Si−9.48Mg−3Cu−1Ni(GC, T6)	101	Re. [39]
Al−11.69Si−3.96Cu−2.00Ni−0.76Mg−0.18Mn−0.14Fe (GC,T6)	69.9	Ref. [40]
Al−12Si−4Cu−2Ni−0.8Mg (GC,T6)	69.9	Ref. [41]

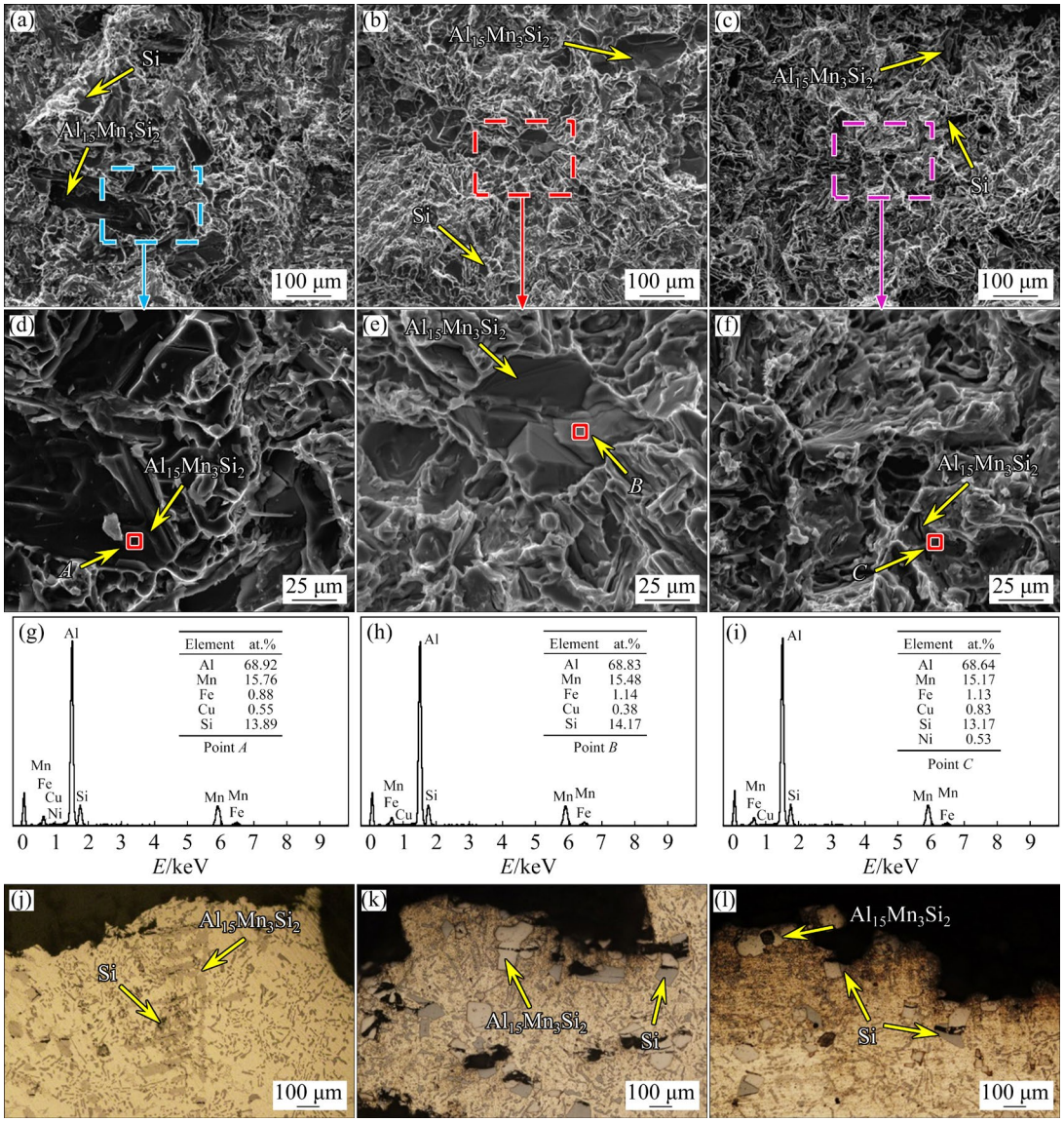

Fig. 13 Fracture surfaces of alloys under different casting methods tested at 350 °C: (a, d) GC treated alloys; (b, e) UV treated alloys; (c, f) UV+MV treated alloys; (g−i) EDS results of Points *A*, *B* and *C*, respectively; (j−l) Fracture surface microstructures along longitudinal direction in GC, UV and UV+MV treated alloys, respectively

that the coarse Mn-rich phases and primary Si particles led to the concentration of stress, providing an easy crack propagation path and eventually causing the fracture of these parts. Several small dimples were found on the fracture surfaces of the UV and UV+MV parts due to the refinement of microstructure, indicating that the ductile fracture mode was more dominant in these parts. Smaller Mn-rich phases and primary Si particles were observed on the fracture surfaces of the UV and UV+MV parts, indicating a lesser stress concentration between the brittle secondary intermetallics and the Al matrix than that of the GC parts. This observation further contributes to the high EL observed in these parts.

Figures 13(j−l) show the fracture surface microstructure along the longitudinal direction. On the fracture surface of the GC alloys, coarse dendritic-shaped Mn-rich phases were observed (Fig. 13(j)). These brittle intermetallics caused the formation and propagation of cracks and, finally, the fracture of the parts. Many primary Si and block-like Mn-rich particles were observed on the fracture surfaces of the UV and UV+MV parts. This observation indicates that the primary Si particles and Mn-rich phases formed weak locations in these parts, facilitating cracks' formation and propagation during tensile loading (Figs. 13(j) and (l)).

4 Discussion

4.1 Refining mechanism of UV

As previously mentioned, the refined and fragmented α(Al) grains were formed in the microstructure of the UV parts (Fig. 5). Moreover, the UV treatment significantly decreased the size of the secondary intermetallics existing in the microstructure of these parts. This refinement mechanism can be attributed to the acoustic streaming flow, cavitation-induced heterogeneous nucleation, and cavitation-induced dendrite fragmentation during UV treatment.

It is widely accepted that the acoustic streaming flow and cavitation-induced effects of the UV treatment are responsible for the refinement of the microstructure. It has been reported that the acoustic streaming flow threshold of the ultrasonic power density (I) is 100 W/cm^2, and the cavitation threshold of the applied sound pressure (P_A) is 0.6−1.0 MPa [42]. The ultrasonic power density (I) and applied sound pressure (P_A) can be respectively calculated by the following equations [42]:

$$I=\frac{1}{2}\rho c\left(2\pi fA\right)^2 \tag{1}$$

$$P_A=\sqrt{\frac{2wc}{S}} \tag{2}$$

where ρ is the density of the Al melt (2.452 g/cm^3 at 620 °C for the Al−12.43Si alloy [43]), c is the speed of sound in the Al melt (4.7×10^5 cm/s [44]), f is the acoustic frequency (20000 Hz), A is the acoustic amplitude (2×10^{-3} cm), w is the useful acoustic power transmitted in Al (900 W), and S is the surface area of the probe (12.56 cm^2). The ultrasonic power density and applied sound pressure were calculated according to Eqs. (1) and (2) and found to be 1164 W/cm^2 and 4 MPa, respectively. These values are much higher than the acoustic streaming flow and cavitation thresholds. In this study, the UV treatment was applied to the liquid and solid regions of the alloys. As a result, the heterogeneous nucleation and dendrite fragmentation caused by acoustic streaming flow and cavitation occurred in the UV samples prepared.

The mechanisms of heterogeneous nucleation of α(Al) grains and secondary intermetallics can be explained from three aspects. First, the acoustic streaming flow benefits the temperature and solute uniformity of the Al melt. According to the pressure pulse-melting point mechanism of the Clapeyron equation, the cavitation bubbles increase the pressure in the Al melt, increasing the melting point. A high melting point is equivalent to an enhanced undercooling, leading to an enhanced nucleation level in the melt. Second, the cavitation bubbles undercool the bubble−liquid interfaces increasing the nucleation rate on the surface. Third, the bubbles can significantly improve the wettability of inclusions, including the $MgAl_2O_4$ and aluminum oxide film. These wetted inclusions act as effective nucleation sites during solidification [45].

The dendrite fragmentation of α(Al) grains and secondary intermetallics can be explained by the acoustic flow effect. It is well acknowledged that the main mechanisms involved in the acoustic flow effect are the re-melting and deflection of dendrites, which have been proven by synchrotron X-ray radiography [46,47].

Certain reports have suggested that the overheating effect of high-frequency UV can lead to the re-melting of dendrites [48]. In addition, ZHANG et al [49] reported that dendrite fragmentation can be attributed to the decreased melting point of the dendrites under applied stress. The latter can be attributed to the curvature re-melting of the dendrites induced by the rapid dendrite growth and the increased free energy caused by their increased internal stress.

As regards the deflection of dendrites, a simple model has been developed by PILLING and HELLAWELL [50] and WANG et al [51] to estimate the mechanical stress caused by the acoustic streaming flow on primary dendrites. The mechanical stress (σ) can be calculated according to the following equation:

$$\sigma=\frac{6\eta VL^2}{r^3} \tag{3}$$

where r is the radius of the dendrite, L is its length, η is the dynamic viscosity, and V is the flow velocity (1.01 m/s; [52]). The viscosity η of the Al−12Si alloy at 620 °C is about 0.93×10^{-3} kg·m^{-1}·s^{-1} [53], the length L of the dendrites is about 2000 μm [54], and their radius r is assumed to be 5−100 μm [51]. The mechanical stress resulting from the acoustic streaming flow on α(Al) dendrite and $Al_{15}Mn_3Si_2$ is given in Fig. 14.

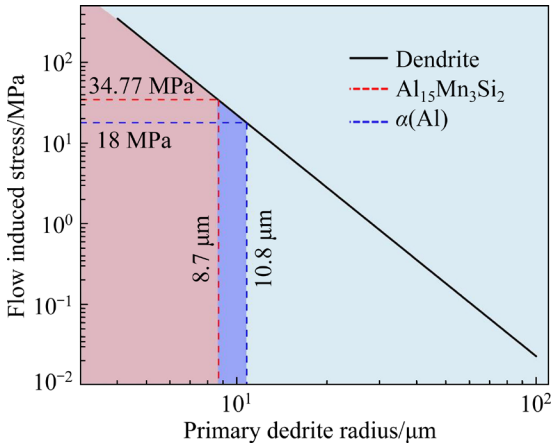

Fig. 14 Acoustic streaming flow on α(Al) dendrite and $Al_{15}Mn_3Si_2$

The YS of α(Al) dendrite at 300 °C is approximately 18 MPa [54]. The YS of the $Al_{15}Mn_3Si_2$ intermetallic at 525 °C is estimated by the method proposed by FROST and ASHBY [55] as follows:

$$\sigma_y = 10^{-3} E(T) \tag{4}$$

$$E(T) = E_{300}\left(1 + B\left(\frac{T-300}{T_m}\right)\right) \tag{5}$$

where σ_y is the yield strength, $E(T)$ is the Young's modulus at temperature (T), E_{300} is the modulus at 300 K, T_m is the melting temperature, and B is the constant. The incipient melting temperature of the $Al_{15}Mn_3Si_2$ intermetallic is around 864 K (625 °C), and the melting temperature is estimated to be approximately 798 K (525 °C) [54]. The E_{300} of the $Al_{15}Mn_3Si_2$ intermetallic has been measured to be 149 GPa [10], and the constant B is taken as −1.33 [50]. According to Eqs. (4) and (5), YS of the $Al_{15}Mn_3Si_2$ intermetallic at 525 °C is calculated to be about 34.77 MPa.

According to Fig. 14, the stress on α(Al) dendrite reaches 18 MPa once its radius is decreased to 10.8 μm, indicating that breaking the α(Al) dendrite is possible by the stress induced by the acoustic streaming flow. At 525 °C, the acoustic streaming flow can deflect the $Al_{15}Mn_3Si_2$ intermetallic dendrites. This observation is attributed to the stress reaching 34.77 MPa, i.e., the calculated YS of the $Al_{15}Mn_3Si_2$ intermetallic, only when the radius r of the dendrites is close to 8.7 μm. Moreover, it is highly possible to deflect the α(Al) and $Al_{15}Mn_3Si_2$ dendrites by the stress induced by the acoustic streaming flow at 620 °C. This is considering the occurrence of concurrent remelting at this temperature, the weak location of the dendrite neck, and the decrease in the YS of the $Al_{15}Mn_3Si_2$ dendrite at high temperatures.

4.2 Passivation or non-dendrite mechanism caused by UV treatment

According to Fig. 7, the UV treatment refined the size of the $Al_{15}Mn_3Si_2$ particles and passivated their edges. Moreover, some of the $Al_{15}Mn_3Si_2$ particles even became non-dendritic in the UV-treated parts (Fig. 7(d)). It has been reported that the growth condition of the dendrites depends on the heat release and solute diffusion changes at the solid−liquid (S−L) interface [56].

The 3D morphology of $Al_{15}Mn_3Si_2$ particles obtained a dendrite shape in the GC alloys (Fig. 7(a)). This indicates that the axes of the dendrites experienced different growth rates. First, the heat release of the growth in the new nuclei of $Al_{15}Mn_3Si_2$ in undercooled unstirred Al melts traverses more easily from the convex surface location than from the concave surface one. Consequently, the convex surface grows faster than the concave one. This crystal anisotropy causes the interface to evolve at different rates and grow preferentially [57]. As a result, the nucleus of $Al_{15}Mn_3Si_2$ grows into a dendritic structure. Moreover, it has been reported that the solute diffusion rate of Mn is very low, which leads to high constitutional supercooling when the cooling rate is slow. This observation ultimately results in the formation of equiaxed dendrites [58]. According to the literature [58], $Al_{15}(MnFe)_3Si_2$ obtains an equiaxed dendrite shape in the GC alloys.

In the UV samples, the forced melt stirring caused by the acoustic flow strongly changes the heat release and solute diffusion, further altering the growth conditions. First, the melt stirring caused by the acoustic flow effect leads to a more uniform temperature distribution at the S−L interfaces; thus, the fluctuation of the S−L interface profile is effectively reduced [59]. Furthermore, the cooling rate and temperature gradients change due to the acoustic streaming. The acoustic flow accelerates the heat transfer in the melt, leading to a higher cooling speed, shorter growth time, and homogeneous growth of the crystal nuclei [60]. These factors are beneficial to preventing the

excessive growth of the dendritic stem and its branches and facilitate the formation of edge passivation or non-dendritic structures.

Furthermore, the crystal growth of the $Al_{15}Mn_3Si_2$ nuclei also depends on the solute diffusion [57]. The forced convection reduces the diversity of the solute diffusion in the different directions at the S−L interface, weakening the preference for dendritic growth. Consequently, the decreased preference for dendritic growth resulting from acoustic streaming can be attributed to heat release and solute diffusion changes. These further induce the formation of edge passivation or even non-dendritic structures in the UV alloys.

4.3 Refining and modification effects of MV treatment

As mentioned above, applying the UV+MV treatment resulted in the formation of refined α(Al) grains and secondary intermetallics in the microstructure of the prepared parts. It is widely accepted that the main mechanisms activated under MV treatments are due to the turbulence and synergetic vibration effects [61]. The refining mechanisms of α(Al) grains and secondary intermetallics under MV treatment can be divided into two types. The first mechanism is related to the uniform cooling temperature of the melts. The turbulent effect can uniformly cool the Al melt and enhance its nucleation. Furthermore, the MV treatment causes the accelerated separation of the grains close to the liquid level and the mold wall. The second mechanism is attributed to the dendrite fragmentation caused by the MV treatment. The fluctuation of the dendrites due to the synergetic vibration effect leads to the development of mechanical stress, which causes dendrite fragmentation. The turbulence effects can promote a relative movement between liquid and solid phases, and the impact of the liquid flow causes the dendrites to break and form the crystal cores. The turbulence effect can also induce solute concentration and temperature elevation in the root region of dendrites or high-order dendrite arms. As a result, the dendrites or dendrite arms break due to root necking.

4.4 Effects of UV and MV treatments on tensile properties at room temperature

According to Fig. 12, the room temperature tensile properties of the UV and UV+MV treated parts were improved compared to those of GC. The improvement of the mechanical properties can be attributed to the refinement and modification of the α(Al) grains and secondary intermetallics.

First, the refinement of the α(Al) grains and secondary intermetallics (mainly the primary Si particles and Mn-rich phases) significantly improves the mechanical properties. According to the Hall−Petch equation, grain refinement improves the tensile properties at room temperature. According to a previous study [62], the refinement of secondary intermetallics can reduce the crack formation between interfacial α(Al) matrix and secondary intermetallics, the stress concentration between secondary intermetallics, and their possible cracking. All these factors further improve the fracture strength of these parts.

In addition, the improvement in the tensile properties at room temperature can also be attributed to the precipitation strengthening resulting from increased dispersoids in the α(Al) matrix. According to Fig. 9, the precipitates in the UV and UV+MV samples were more abundant and more homogeneously distributed than those in the GC samples, which can be beneficial to preventing dislocation movement. Moreover, the nano-sized Si particles and degassing effect from the UV and MV treatments have significantly improved the tensile properties at room temperature.

4.5 Effects of UV and MV treatments on elevated temperature tensile properties and creep resistance

The UV and UV+MV treatments improved the tensile properties at the temperature of 350 °C and the creep resistance of the investigated parts compared to those of the GC alloys. Surprisingly, compared to the UV parts, the UV+MV-treated Al−Si−Cu−Ni−Mg−Mn parts exhibited a lower tensile strength at elevated temperatures.

An efficient method to improve the elevated temperature tensile properties and creep resistance of the heat-resistant Al alloys is to prevent the movement of dislocations in the α(Al) and grain boundary sliding by forming heat-resistant phases in the microstructure [63]. In this study, refined α(Al) grains, secondary intermetallics, and increased heat-resistant precipitates were found in the microstructure of both the UV and UV+MV

parts. It is widely accepted that the Al_2Cu phase is stable at 200 °C, while the Si particles, Mn-rich phases ($Al_{15}Mn_3Si_2$, $Al_{11}Cu_5Mn_3$, and $Al_{20}Cu_2Mn_3$), and Al_3(CuNi) phases are considered thermally stable below 350−400 °C [64]. It has been reported that the suitable refinement of grains and the formation of heat-resistant secondary intermetallics and their precipitates are beneficial for improving elevated temperature tensile properties and creep resistance of Al alloys [65]. However, the connectivity ability of the heat-resistant phase network structure also plays a significant role in the elevated temperature tensile properties [66]. In this study, connectivity of the network structure of the heat-resistant particles in the UV parts was achieved. These parts exhibited high tensile strength at elevated temperatures. On the other hand, in the UV+MV alloys, the over-refinement of the α(Al) grains and secondary intermetallics destroyed the connectivity of the network structure of the heat-resistant phases. Consequently, these parts exhibited inferior tensile strength at elevated temperatures compared to the UV ones.

The microstructure evolution of the Al−Si−Cu−Ni−Mg−Mn alloys processed under different casting conditions is illustrated in Fig. 15. Overall, the refinement and passivation of the microstructures have played a vital role in the improved mechanical properties of the UV- and UV+MV-treated parts.

5 Conclusions

(1) The UV and UV+MV treatments successfully refined the α(Al) grains, primary Si particles, and Mn-rich intermetallic $Al_{15}Mn_3Si_2$ phase. The refinement mechanism can be attributed to the heterogeneous nucleation and dendrite fragmentation induced by the acoustic streaming flow and cavitation effects of UV and turbulence and synergetic vibration effects of MV.

(2) The 3D morphologies of the secondary intermetallics existing in the microstructure were reconstructed by SXCT. The $Al_{15}Mn_3Si_2$ in GC parts exhibited an equiaxed dendrite shape, and the $Al_{15}Mn_3Si_2$ in UV parts exhibited edge passivation or even non-dendrite shapes. The latter can be attributed to the changes in the heat release and solute diffusion induced by acoustic streaming, reducing the preferred crystallographic growth.

(3) Two types of nano-sized block-like precipitates, i.e., $Al_{15}Mn_3Si_2$ and $Al_{11}Cu_5Mn_3$, were found in the Al−Si−Cu−Ni−Mg−Mn parts. Both precipitates possess high heat resistance, which is beneficial to improving the mechanical properties.

(4) Compared to the GC alloys, the UV- and UV+MV-treated parts exhibited improved tensile properties at room and elevated temperatures and creep resistance. This improvement in the mechanical

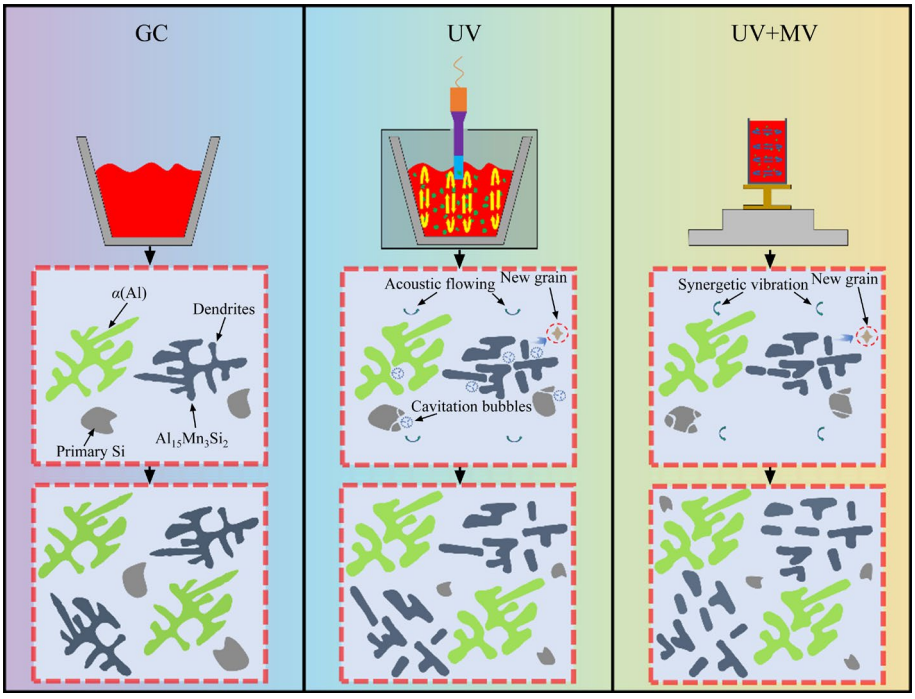

Fig. 15 Microstructure evolution of alloys under different casting conditions

properties can be attributed to the refinement of the α(Al) grains and secondary intermetallics, the refined and increased level of heat-resistance precipitates, and the nano-sized Si particles. The UTS of the UV parts at the elevated temperature of 350 °C was 113 MPa, which was superior to that of commercial Al−Si piston alloys.

(5) The over-refinement of the α(Al) grains and secondary intermetallics and the weaker connectivity of the network structure of the heat-resistant phases in the UV+MV parts led to a lower tensile strength at the elevated temperature of 350 °C compared to that of the UV alloys. The results of this study emphasize that optimizing the refinement process of the α(Al) grains and secondary intermetallics formed in the micro-structure of Al−Si piston alloys is essential to obtain superior mechanical properties.

CRediT authorship contribution statement

Bo LIN: Conceptualization, Methodology, Investigation, Resources, Writing – Original draft preparation, Supervision, Funding acquisition; **Xiang-xiang HE:** Conceptualization; **Song-chao XIA:** Software, Validation; **Hua-qiang XIAO:** Validation, data curation; **Yu-liang ZHAO:** Validation, Formal analysis; **Khashayar KHANLARI:** Software, Writing – Review & editing.

Declaration of competing interest

The authors declare that they have no known competing financial interests or personal relationships that could have appeared to influence the work reported in this paper.

Acknowledgments

This work was funded by the National Natural Science Foundation of China (No. 52265043), Science and Technology Plan, Guizhou Province, China (No. ZK2021(267)), Technology Achievements Application and Industrialization Project, Guizhou Province, China (No. 2021(067)), and Cultivation Project of Guizhou University, China (No. 2019(23)). Lastly, we thank the Shanghai Synchrotron Radiation Facility (SSRF) for providing the synchrotron radiation beamtime.

References

[1] LIU H Q, PANG J C, WANG M, LI S X, ZHANG Z F. Effect of temperature on the mechanical properties of Al−Si−Cu−Mg−Ni−Ce alloy [J]. Materials Science and Engineering A, 2021, 824: 141762.

[2] LIU Yan-yu, JIA Li-na, WANG Wen-bo, JIN Zu-heng, ZHANG Hu. Effects of Ni content on microstructure and wear behavior of Al−13Si−3Cu−1Mg−xNi−0.6Fe−0.6 Mn alloys [J]. Wear, 2022, 500: 204365.

[3] DEMIRTAŞ H, KARAKULAK E, BABU N H. Understanding the effect of Ni content on microstructure and mechanical properties of A384 HPDC alloy [J]. Journal of Alloys and Compounds, 2022, 896: 163111.

[4] WANG M, PANG J C, ZHANG M X, LIU H Q, LI S X, ZHANG Z F. Thermo-mechanical fatigue behavior and life prediction of the Al−Si piston alloy [J]. Materials Science and Engineering A, 2018, 715: 62−72.

[5] TIAN Lu-sha, GUO Yong-chun, LI Jian-ping, WANG Jian-li, DUAN Hong-bo, XIA Feng, LIANG Min-xian. Elevated re-aging of a piston aluminium alloy and effect on the microstructure and mechanical properties [J]. Materials Science and Engineering: A, 2018, 738: 375−379.

[6] LIAO Heng-cheng, TANG Yun-yi, SUO Xiao-jing, LI Guang-jin, HU Yi-yun, DIXIT U S, PETROV P. Dispersoid particles precipitated during the solutionizing course of Al−12wt.%Si−4wt.%Cu−1.2wt.%Mn alloy and their influence on high temperature strength [J]. Materials Science and Engineering: A, 2017, 699: 201−209.

[7] LIU K, CHEN X G. Improvement in elevated- temperature properties of Al−13%Si piston alloys by dispersoid strengthening via Mn addition [J]. Journal of Materials Research, 2018, 33(20): 3430−3438.

[8] LIAO Heng-cheng, XU He-ting, HU Yi-yuan. Effect of RE addition on solidification process and high-temperature strength of Al−12%Si−4%Cu−1.6%Mn heat-resistant alloy [J]. Transactions of Nonferrous Metals Society of China, 2019, 29(6): 1117−1126.

[9] LI Guang-jing, LIAO Heng-cheng. E2EM's prediction of LaB_6 as nucleation substrate for primary Mn-rich phase in Al−Si−Cu−Mn heat-resistant alloy and its refining effect [J]. Transactions of Nonferrous Metals Society of China, 2022, 32(6): 1795−1804.

[10] LI Guang-jing, LIAO Heng-cheng, XU Ai. Two quite different primary Mn-rich phases in Al−Si−Cu−Mn heat- resistant alloy and its effect to mechanical properties [J]. Materials Science and Engineering A, 2018, 730: 36−40.

[11] LI Guang-jin, LIAO Heng-cheng, SUO Xiao-jing, TANG Yun-yi, DIXIT U S, PETROV P. Cr-induced morphology change of primary Mn-rich phase in Al−Si−Cu−Mn heat resistant aluminum alloys and its contribution to high temperature strength [J]. Materials Science and Engineering A, 2018, 709: 90−96.

[12] LIN Bo, XIA Song-chao, TANG Yue, ZHAO Yu-liang, LIU Kun, XIAO Hua-qiang, LI Shao-bo, ZHANG Wei-wen. Effects of thermal exposure on the microstructure and mechanical properties of Al−12Si−4Cu−1Ni−1Mg−2Mn piston alloys [J]. International Journal of Cast Metals Research, 2020, 33(6): 250−257.

[13] QI Ming-fan, XU Yu-zhao, LI Jing-yuan, KANG Kong-lin, WULABIEKE Z. Microstructure refinement and corrosion resistance improvement mechanisms of a novel Al−Si−Fe−Mg−Cu−Zn alloy prepared by ultrasonic vibration-assisted

rheological die-casting process [J]. Corrosion Science, 2021, 180: 109180.

[14] YADAV S, TEWARI S P, SINGH J K, RAM S C. Effects of mechanical vibration on the physical, metallurgical and mechanical properties of cast A308 (LM21) aluminum alloy [J]. International Journal of Minerals, Metallurgy and Materials, 2022, 29(6): 1206−1215.

[15] JUNG J G, LEE S H, LEE J M, CHO Y H, KIM S H, YOON W H. Improved mechanical properties of near-eutectic Al−Si piston alloy through ultrasonic melt treatment [J]. Materials Science and Engineering A, 2016, 669: 187−195.

[16] JUNG J G, LEE J M, CHO Y H, YOON W H. Combined effects of ultrasonic melt treatment, Si addition and solution treatment on the microstructure and tensile properties of multicomponent Al−Si alloys [J]. Journal of Alloys and Compounds, 2017, 693: 201−210.

[17] JUNG J G, LEE S H, CHO Y H, YOON W H, AHN T Y, AHN Y S, LEE J M. Effect of transition elements on the microstructure and tensile properties of Al−12Si alloy cast under ultrasonic melt treatment [J]. Journal of Alloys and Compounds, 2017, 712: 277−287.

[18] DONG Xiong-bo, GUO Yong-chun, LI Jian-ping, WANG Jian-li, XIA Feng, MA Zhi-jun, YANG Wei, BAI Ya-ping, LIANG Min-xian. Influence of ultrasonic melt treatment on Ni-containing intermetallic phases in Al−Si piston alloys [J]. Advanced Engineering Materials, 2020, 22(12): 1901590.

[19] ABU-DHEIR N, KHRAISHEH M, SAITO K, MALE A. Silicon morphology modification in the eutectic Al−Si alloy using mechanical mold vibration [J]. Materials Science and Engineering A, 2005, 393(1/2): 109−117.

[20] BABU N R, RAMESH M R, AITHAL S K, KOTRESH K. Effect of lateral vibrations during directional solidification on mechanical properties of Al−18wt.%Si alloys [J]. Materials Today: Proceedings, 2018, 5(2): 6954−6962.

[21] ZHAO Yu-liang, ZHANG Wei-wen, SONG Dong-fu, LIN Bo, SHEN Fang-hua, ZHENG Dong-hai, XIE Chun-xiao, SUN Zhen-zhong, FU Ya-nan, LI Run-xia. Nucleation and growth of Fe-rich phases in Al−5Ti−1B modified Al−Fe alloys investigated using synchrotron X-ray imaging and electron microscopy [J]. Journal of Materials Science & Technology, 2021, 80: 84−99.

[22] ZHAO Yu-liang, SONG Dong-fu, WANG Hao-liang, LI Xin-xin, CHEN Li-jia, SUN Zhen-zhong, WANG Zhi, ZHAI Tong-guang, FU Ya-nan, WANG Yao, LIU Shu-hong, DU Yong, ZHANG Wei-wen. Revealing the nucleation and growth mechanisms of Fe-rich phases in Al−Cu−Fe(−Si) alloys under the influence of Al−Ti−B [J]. Intermetallics, 2022, 146: 107584.

[23] LI Guang-jing, LIAO Heng-cheng, XU Ai-qun, TANG Jing-fan, ZHAO Bao-jun. Peritectic reaction between two primary Mn-rich phases during solidification of Al−Si−Cu−Mn heat-resistant alloy and the effect of cooling rate on it [J]. Journal of Alloys and Compounds, 2018, 753: 239−246.

[24] LI Guang-jing, LIAO Heng-cheng, ZHENG Ji-wei, CHEN Hui, QIAN Long-jie, YANG Mo-tong, LU Li-zhen, SHI Meng-chuan. Sc-induced great increase in high temperature strength of Al−Si−Cu heat-resistant alloy [J]. Journal of Alloys and Compounds, 2022, 925: 166622.

[25] AKOPYAN T K, BELOV N A, LETYAGIN N V, MILOVICH F O, LUKYANCHUK A A, FORTUNA A S. Influence of indium trace addition on the microstructure and precipitation hardening response in Al−Si−Cu casting aluminum alloy [J]. Materials Science and Engineering A, 2022, 831: 142329.

[26] ZHANG Jia-yu, ZUO Li-jie, FENG Jian, YE Bing, KONG Xiang-yang, JIANG Hai-yan, DING Wen-jiang. Effect of thermal exposure on microstructure and mechanical properties of Al−Si−Cu−Ni−Mg alloy produced by different casting technologies [J]. Transactions of Nonferrous Metals Society of China, 2020, 30(7): 1717−1730.

[27] XU Da-zhao, MENG Ling-gang, ZHANG Chang-ri, CHEN Xi, ZHANG Xing-guo. Interface microstructure evolution and bonding mechanism during vacuum hot pressing bonding of 2A12 aluminum alloy [J]. Materials Characterization, 2022, 189: 111997.

[28] CHEN Y Q, TANG Z H, PAN S P, LIU W H, SONG Y F, LIU Y, ZHU B W, ZHOU W, SHEN F H. A new type of anti-phase boundaries in the $T(Al_{20}Cu_2Mn_3)$ phase and the pre-deformation effect on T phase precipitation [J]. Intermetallics, 2020, 127: 106977.

[29] WANG E R, HUI X D, CHEN G L. Eutectic Al−Si−Cu−Fe−Mn alloys with enhanced mechanical properties at room and elevated temperature [J]. Materials & Design, 2011, 32(8/9): 4333−4340.

[30] XU Rui, LIN Bo, LI Hao-yu, XIAO Hua-qiang, ZHAO Yu-liang, ZHANG Wei-wen. Microstructure evolution and mechanical properties of Al−6.5Cu−0.6Mn−0.5Fe alloys with different Si additions [J]. Transactions of Nonferrous Metals Society of China, 2019, 29: 1583−1591.

[31] PAN Shi-wei, QIAN Feng, LI Chuan, WANG Zi-dong, LI Yan-jun. Synergistic strengthening by nano-sized α-Al (Mn, Fe) Si and Al_3Zr dispersoids in a heat-resistant Al−Mn−Fe−Si−Zr alloy [J]. Materials Science and Engineering A, 2021, 819: 141460.

[32] LI Jian-yu, LÜ Shu-lin, ZHAO Di-jia, CHEN Lu, PAN Yu, GUO Wei, WU Shu-sen. Preparation of Mg_2Si/Al−Cu composite under a novel continuous squeeze casting-extrusion process assisted with ultrasonic treatment [J]. Materials Science and Engineering A, 2023, 862: 144469.

[33] PENG Nan-hui, ZHAN Li-hua, SONG Ze-tian, ZHU Wen-li, XU Yong-qian, MA Lin-bo, ZENG Quan-qing, CHEN Kai. LAO Shan-feng, ZHENG Qi. Strengthening mechanism of 2219 Al−Cu alloy by room-temperature random vibration [J]. Journal of Alloys and Compounds, 2023, 934: 167878.

[34] WANG Tao, CHEN Xiao-hua, LUO Xiang, JIANG Han, CHEN Ming-wen, WANG Zi-dong. Formation of Si nanoparticle in Al matrix for Al−7wt.%Si alloy during complex shear flow casting [J]. Journal of Alloys and Compounds, 2018, 739: 30−34.

[35] LI Yun-guo, YANG Yang, WU Yu-ying, WANG Li-yan, LIU Xiang-fa. Quantitative comparison of three Ni-containing phases to the elevated-temperature properties of Al−Si piston alloys [J]. Materials Science and Engineering A, 2010, 527(26): 7132−7137.

[36] QIAN Zhao, LIU Xiang-fa, ZHAO De-gang, ZHANG Guo-hua. Effects of trace Mn addition on the elevated temperature tensile strength and microstructure of a low-iron

Al−Si piston alloy [J]. Materials Letters, 2008, 62(14): 2146−2149.

[37] ZUO Li-jie, YE Bing, FENG Jian, KONG Xiang-yang, JIANG Hai-yan, DING Wen-jiang. Microstructure, tensile properties and creep behavior of Al−12Si−3.5Cu−2Ni−0.8Mg alloy produced by different casting technologies [J]. Journal of Materials Science & Technology, 2018, 34(7): 1222−1228.

[38] FENG Jian, YE Bing, ZUO Li-jie, QI Ru-juan, WANG Qu-dong, JIANG Hai-yan, HUANG Rong, DING Wen-jiang. Effects of Ni content on low cycle fatigue and mechanical properties of Al−12Si−0.9Cu−0.8Mg−*x*Ni at 350 °C [J]. Materials Science and Engineering A, 2017, 706: 27−37.

[39] SUN Yi-lin, LI Chong, LIU Yong-chang, DING Ran, LIU Xiang-fa, KIM S H, YU Li-ming. The contribution of aluminides to strength of Al−Mg_2Si−Cu−Ni alloys at room and elevated temperatures [J]. Materials Science and Engineering A, 2021, 817: 141381.

[40] HAN Li-na, SUI Yu-dong, WANG Qu-dong, WANG Kui, JIANG Ye-hua. Effects of Nd on microstructure and mechanical properties of cast Al−Si−Cu−Ni−Mg piston alloys [J]. Journal of Alloys and Compounds, 2017, 695: 1566−1572.

[41] TAN Pan, YANG Yi, SUI Yu-dong, WANG Qu-dong, JIANG Ye-hua. The influence of Al−10Sr or/and Al−5Ti−1B on microstructure and mechanical properties of Al−12Si−4Cu−2Ni−0.8Mg alloys [J]. Journal of Alloys and Compounds, 2019, 809: 151856.

[42] ESKIN G I, ESKIN D G. Ultrasonic treatment of light alloys melts [M]. Boca Raton: CRC Press, 2014.

[43] SCHMITZ J, HALLSTEDT B, BRILLO J, EGRY I, SCHICK M. Density and thermal expansion of liquid Al−Si alloys [J]. Journal of Materials Science, 2012, 47(8): 3706−3712.

[44] BLAIRS S. Sound velocity of liquid metals and metalloids at the melting temperature [J]. Physics and Chemistry of Liquids, 2007, 45: 399−407.

[45] WANG Yun, LI Hu-tian, FAN Zhong-yun. Oxidation of aluminium alloy melts and inoculation by oxide particles [J]. Transactions of the Indian Institute of Metals, 2012, 65(6): 653−661.

[46] LIOTTI E, LUI A, KUMAR S, GUO Z, BI C, CONNOLLEY T, GRANT P S. The spatial and temporal distribution of dendrite fragmentation in solidifying Al−Cu alloys under different conditions [J]. Acta Materialia, 2016, 121: 384−395.

[47] ZHANG Zhi-guo, WANG Chuang-nan, KOE B, SCHLEPÜTZ C M, LRVINE S, MI Jia-wei. Synchrotron X-ray imaging and ultrafast tomography in situ study of the fragmentation and growth dynamics of dendritic microstructures in solidification under ultrasound [J]. Acta Materialia, 2021, 209: 116796.

[48] WANG S, KANG J, ZHANG X, GUO Z. Dendrites fragmentation induced by oscillating cavitation bubbles in ultrasound field [J]. Ultrasonics, 2018, 83: 26−32.

[49] ZHANG A, DU J L, GUO Z P, WANG Q G, XIONG S M. A phase-field lattice-Boltzmann study on dendritic growth of Al−Cu alloy under convection [J]. Metallurgical and Materials Transactions B, 2018, 49(6): 3603−3615.

[50] PILLING J, HELLAWELL A. Mechanical deformation of dendrites by fluid flow [J]. Metallurgical and Materials Transactions A, 1996, 27: 229−232.

[51] WANG Feng, ESKIN D, MI Jia-wei, WANG Chuang-nan, KOE B, KING A, REINHARD C, CONNOLLEY T. A synchrotron X-radiography study of the fragmentation and refinement of primary intermetallic particles in an Al−35Cu alloy induced by ultrasonic melt processing [J]. Acta Materialia, 2017, 141: 142−153.

[52] LIN B, LIN C H, FAN T, ZHANG Y, ZHANG W W. Effect of ultrasound vibration and pressure coupling field on function mechanism and microstructure of Al−Cu alloy [J]. The Chinese journal of Nonferrous Metals, 2021, 31(7): 1818−1826. (in Chinese)

[53] POIRIER D R. Density, viscosity, and diffusion coefficients in hypoeutectic Al−Si liquid alloys: An assessment of available data [J]. Metallurgical and Materials Transactions B, 2014, 45(4): 1345−1354.

[54] SVERDLIN A, GEORGE E, TOTTEN Y D. Properties of pure aluminum [M]//Encyclopedia of Aluminum and Its Alloys. Boca Raton: CRC Press, 2018: 2060−2089.

[55] ATKINS A G. Deformation-mechanism maps (the plasticity and creep of metals and ceramics) [J]. Journal of Mechanical Working Technology, 1984, 9(2): 224−225.

[56] FENG Xiao-hui, ZHAO Fu-ze, JIA Hong-min, LI Ying-ju, YANG Yuan-sheng. Numerical simulation of non-dendritic structure formation in Mg−Al alloy solidified with ultrasonic field [J]. Ultrasonics Sonochemistry, 2018, 40: 113−119.

[57] KURZ W, FISHER D J. Fundamentals of Solidification [M]. Switzerland: Trans Tech Publications Ltd, 2023: 297−309.

[58] LIU K, CAO X, CHEN X G. Solidification of iron-rich intermetallic phases in Al−4.5Cu−0.3Fe cast alloy [J]. Metallurgical and Materials Transactions A, 2011, 42(7): 2004−2016.

[59] TAN D Y, LEE T L, KHONG J C, CONNOLLEY T, FEZZAA K, MI J W. High-speed synchrotron X-ray imaging studies of the ultrasound shockwave and enhanced flow during metal solidification processes [J]. Metallurgical and Materials Transactions A, 2015, 46: 2851−2861.

[60] FENG X H, ZHAO F Z, JIA H M, ZHOU J X, LI Y D, LI W R, YANG Y S. Effect of temperature conditions on grain refinement of Mg−Al alloy under ultrasonic field [J]. International Journal of Cast Metals Research, 2017, 30(6): 341−347.

[61] CAMPBELL J. Effects of vibration during solidification [J]. International Metals Reviews, 1981, 26(1): 71−108.

[62] LIN Bo, XU Rui, LI Hao-yu, XIAO Hua-qiang, ZHANG Wei-wen, LI Shao-bo. Development of high Fe content squeeze cast 2A16 wrought Al alloys with enhanced mechanical properties at room and elevated temperatures [J]. Materials Characterization, 2018, 142: 389−397.

[63] LIN B, XIA S C, LI H Y, LOU Z H, LIU K, ZHANG W W. Improved creep resistance of Al−Cu−Mn−Fe−Ni alloys through squeeze casting [J]. Materials Characterization, 2019, 158: 109935.

[64] CHEN C L, WEST G D, THOMSON R C. Characterisation of intermetallic phases in multicomponent Al−Si casting alloys for engineering applications [J]. Materials Science Forum, 2006, 519/520/521: 359−364.

[65] YANG Y. Study on the evolution and collaborative strengthing mechanism of heat-resistant phases in multicomponent Al−Si alloy [D]. Jinan: Shandong University, 2013. (in Chinese)
[66] BUGELNIG K, SKET F, GERMANN H, STEFFENS T, KOOS R, WILDE F, BOLLER E, REQUENA G. Influence of 3D connectivity of rigid phases on damage evolution during tensile deformation of an AlSi12Cu4Ni2 piston alloy [J]. Materials Science and Engineering A, 2018, 709: 193−202.

超声和机械振动对 Al−12Si−4Cu−1Ni−1Mg−2Mn 活塞合金中富 Mn 相的演变及其力学性能的影响

林 波[1]，何项项[1]，夏松超[1]，肖华强[1]，赵愈亮[2,3]，Khashayar KHANLARI[4]

1. 贵州大学 机械工程学院，贵阳 550025；
2. 东莞理工大学 机械工程学院，东莞 523808；
3. Centro Nacional de Investigaciones Metalúrgicas (CENIM), C.S.I.C., Avda. de Gregorio del Amo 8, Madrid 28040, Spain;
4. Department of Chemical & Biotechnological Engineering, Université de Sherbrooke, Québec, QC J1K 2R1, Canada

摘　要：研究超声振动(UV)和机械振动(MV)对 Al−12Si−4Cu−1Ni−1Mg−2Mn 活塞合金中富 Mn 相演变及其力学性能的影响。结果表明，UV 和 UV+MV 处理能显著细化和破碎合金的显微组织，且 UV 处理可以明显钝化初生富 Mn 金属间化合物 $Al_{15}Mn_3Si_2$ 相，并详细分析晶粒细化、钝化以及非枝晶颗粒的形成机理。与重力铸造的合金相比，经 UV 和 UV+MV 处理的合金在室温和高温下都表现出优异的拉伸性能和抗蠕变性能，这可归因于 α(Al)晶粒和金属间化合物的细化、细小的耐热析出相比例增加以及纳米 Si 颗粒的形成。在 350 ℃下，经 UV 处理合金的极限抗拉强度超过商用活塞合金，这表明所研制的活塞合金在高功率柴油机上具有很大的应用潜力。

关键词：铝硅活塞合金；富 Mn 相；力学性能；超声振动；机械振动

(Edited by Xiang-qun LI)